Neuron

Article

Feedforward mechanisms of cross-orientation interactions in mouse V1

Graphical abstract

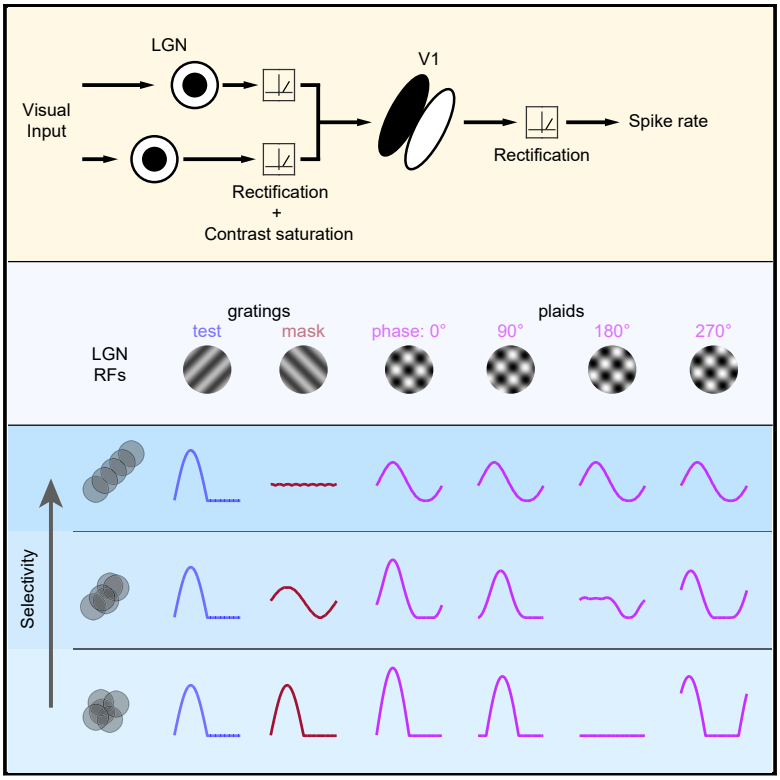

Highlights

- Plaids drive both suppression and facilitation in populations of mouse V1 neurons
- Functional inactivation of cortex does not alter modulation by mask gratings
- The effects of the mask grating depend on stimulus phase in weakly tuned neurons
- The geometry of feedforward inputs defines cross-orientation interactions

Authors

Dylan Barbera, Nicholas J. Priebe, Lindsey L. Glickfeld

Correspondence

nico@austin.utexas.edu (N.J.P.), glickfeld@neuro.duke.edu (L.L.G.)

In brief

Cross-orientation interactions result in diverse effects in mouse V1. Barbera et al. use a combination of calcium imaging, electrophysiology, and modeling to reveal that this heterogeneity can be explained by a single feedforward mechanism: plaids can drive facilitation or suppression depending on alignment with the neurons' receptive fields.

Barbera et al., 2022, Neuron *110*, 297–311
January 19, 2022
https://doi.org/10.1016/j.neuron.2021.10.017

CellPress

Neuron

CellPress

Article

Feedforward mechanisms of cross-orientation interactions in mouse V1

Dylan Barbera,[1] Nicholas J. Priebe,[1,3,*] and Lindsey L. Glickfeld[2,3,4,*]
[1]Center for Learning and Memory, The University of Texas at Austin, 2415 Speedway, Austin, TX 78712, USA
[2]Department of Neurobiology, Duke University Medical Center, Durham, NC 27710, USA
[3]These authors contributed equally
[4]Lead contact
*Correspondence: nico@austin.utexas.edu (N.J.P.), glickfeld@neuro.duke.edu (L.L.G.)
https://doi.org/10.1016/j.neuron.2021.10.017

SUMMARY

Sensory neurons are modulated by context. For example, in mouse primary visual cortex (V1), neuronal responses to the preferred orientation are modulated by the presence of superimposed orientations ("plaids"). The effects of this modulation are diverse; some neurons are suppressed, while others have larger responses to a plaid than its components. We investigated whether this diversity could be explained by a unified circuit mechanism. We report that this masking is maintained during suppression of cortical activity, arguing against cortical mechanisms. Instead, the heterogeneity of plaid responses is explained by an interaction between stimulus geometry and orientation tuning. Highly selective neurons are uniformly suppressed by plaids, whereas the effects in weakly selective neurons depend on the spatial configuration of the stimulus, transitioning systematically between suppression and facilitation. Thus, the diverse responses emerge as a consequence of the spatial structure of feedforward inputs, with no need to invoke cortical interactions.

INTRODUCTION

As information propagates along the visual pathway, neural circuitry makes fundamental transformations in the representation of the visual scene. There are conflicting views on the roles that feedforward and recurrent cortical circuitry play in generating cortical representations of the visual scene (Carandini and Heeger, 2011; Priebe and Ferster, 2012; Alitto and Dan, 2010). It is clear that the intricate recurrent cortical circuitry modifies representations (Hubel and Wiesel, 1962; Nelson and Frost, 1978; Gilbert and Wiesel, 1990), but the convergent inputs from the thalamus also play an essential role in the emergence of cortical selectivity (Chapman et al., 1991; Reid and Alonso, 1995; Ferster et al., 1996; Jin et al., 2011; Lien and Scanziani, 2013). Parsing the contributions of these circuit elements is particularly interesting when multiple stimuli are presented, as cortical responses to these stimuli are often nonlinear. One such phenomena is cross-orientation suppression, a form of masking whereby a neuron's response to an optimally oriented grating is reduced when overlaid by a second grating at an angle other than the preferred orientation, forming a plaid (Blakemore and Tobin 1972; Bonds 1989; Carandini and Heeger 1994; Carandini et al., 1997; DeAngelis et al., 1992; Heeger 1992; Morrone et al., 1982, 1987; Sengpiel et al., 1998).

The orientation specificity of masking has led to mechanistic accounts that rely on the interaction between neurons in visual cortex, where orientation selectivity emerges. In cortical accounts, activated pools of cortical neurons mutually suppress one another through recurrent inhibition (Heeger, 1992; Rubin et al., 2015). The presence of two differently oriented stimuli elicits responses (at least transiently) from a larger pool of neurons than either stimulus does alone, resulting in a reduced response. Alternative accounts consider how plaids alter the afferent input to the cortex. Afferent models note that the geometry of the plaid stimulus alters the timing and amplitude of thalamic responses; some afferent responses are reduced, while others are enhanced. These thalamic responses are then transformed by both thalamic and cortical nonlinearities, including response rectification, contrast saturation, synaptic depression, and the spike threshold nonlinearity, resulting in suppression (Carandini et al., 2002; Freeman et al., 2002; Priebe and Ferster 2006; Li et al., 2006; Koelling et al., 2008).

While cross-orientation suppression is pervasive in cat primary visual cortex (V1; DeAngelis et al., 1992; Priebe and Ferster, 2006), the impact of orthogonal stimuli is more heterogeneous in mice and primates (Juavinett and Callaway, 2015; Muir et al., 2015, 2017; Palagina et al., 2017; Ringach, 2019; Guan et al., 2020). Although many mouse and primate V1 neurons exhibit robust cross-orientation suppression, some neurons exhibit increased responses when the mask is overlaid. Current accounts for cross-orientation interactions provide explanations for suppression, but not facilitation (Heeger, 1992; Rubin et al., 2015; Priebe and Ferster, 2006; Li et al., 2006; Koelling et al., 2008). The mouse visual system therefore provides an

opportunity to address whether a common circuit can explain both cross-orientation suppression and facilitation.

We aim to uncover the mechanisms governing the responses to overlapping gratings in mouse V1 using *in vivo* whole-cell recordings and two-photon calcium imaging. In line with previous reports, we found a broad range of interactions among cortical pyramidal cells, ranging from cross-orientation suppression to facilitation. We demonstrate that both functional (by sensory adaptation) and optogenetic lesions of V1 activity have little effect on the response profile of V1 neurons to plaids, indicating that a cortical mechanism of masking is unlikely. We also directly assayed how masking manifests in parvalbumin-positive (PV^+) cortical interneurons and found that they do not contain signals necessary to support both enhancement and suppression. Instead, we demonstrate from a feedforward model that the heterogeneous nature of V1 responses can be explained by the diversity of orientation selectivity in mouse V1. In neurons with high orientation selectivity, effects are dominated by cross-orientation suppression. However, when orientation selectivity is low, responses can be facilitated or suppressed depending on the spatial phase of the plaid. We then demonstrate that by shifting the phase of the plaid, neuronal responses in low-orientation-selective neurons systematically shift between cross-orientation facilitation and suppression. Therefore, the diverse responses of mouse V1 neurons to plaid stimuli are succinctly accounted for by spatial structure of the feedforward afferents.

RESULTS

To measure the interactions between superimposed oriented gratings in V1 of awake mice, we measured GCAMP6 calcium signals from genetically identified pyramidal cells using a two-photon microscope while presenting single drifting gratings (30-degree diameter with a Gabor mask) of the preferred direction and superimposed orthogonal direction (plaids; Figure 1A). As previously reported, neurons varied widely in their responses to plaid stimuli (Juavinett and Callaway, 2015; Muir et al., 2015, 2017; Palagina et al., 2017; Tring and Ringach, 2018). At one end of the spectrum are neurons whose responses resemble those seen in cats, exhibiting robust decreases in response amplitude to the plaid stimulus compared to their preferred grating alone (Figure 1B, left panel). Within the same field of view, other neurons have larger responses to the plaid stimulus than to the single gratings (Figure 1B, right panel) or exhibit little, if any, change in response amplitude with the addition of a mask (Figure S1A).

To quantify the interaction between grating components, we computed the masking index (MI; Guan et al., 2020):

$$Masking\ Index = \frac{Plaid - (Test + Mask)}{Plaid + (Test + Mask)}$$

An MI below 0 indicates that the response to the plaid is weaker than that expected by the summed responses to the two grating components (suppression), whereas an MI above 0 indicates facilitation. Although facilitation is present and somewhat common, neurons are on average suppressed in response to plaids (normalized change in fluorescence [dF/F] MI: −0.44 ± 0.01; n = 7 mice, 1,426 cells; Figure 1C).

We also find diversity in the effects of masking using whole-cell recordings in layers 2/3 and 4 of anesthetized mice (Figure 1D; for whole-cell recordings, the spatial frequency and size that evoked the largest response for each neuron were used). Electrophysiological records of both membrane potential and spiking have similar patterns of modulations in response to plaids, with examples of both suppression (Figures 1E and 1F, left panel) and facilitation (Figures 1E and 1F, right panel). To quantify these effects, we computed the MI for the modulation component (F1) of the cycle average (MI computed for highest contrast condition – membrane potential: −0.20 ± 0.04; spike rate: −0.21 ± 0.05; n = 28 cells; Figures 1G and 1H). Of the 28 total neurons in the dataset, 16 were recorded in layers 2/3 and 12 were from layer 4. There are no significant differences in MI between the two layers for either membrane potential (unpaired t test, p = 0.50) or spike rate (p = 0.26), suggesting that any difference in masking responses between these layers is minor. Masking is evident to a similar degree in the modulation amplitude (F1, see above), mean amplitude (DC, mean membrane potential MI: −0.24 ± 0.06; mean spike rate MI: −0.28 ± 0.05), and their sum (F1 + DC, membrane potential MI: −0.21 ± 0.04; spike rate MI: −0.25 ± 0.05) in electrophysiological recordings (Figures S1B and S1C). This similarity is likely the reason that the calcium data, which reflect a transformation of the summed activity, match the electrophysiology data.

Some previous studies have found that facilitation is more common than we report here (Juavinett and Callaway, 2015; Muir et al., 2015; Palagina et al., 2017; Ringach, 2019). One possibility is that this may be due to how the orientation of the test and mask gratings are defined. In our dataset, the test stimulus is defined as the preferred orientation. Other studies, however, have not used this criterion, and the test stimulus may or may not be at the preferred orientation of the neuron, and this alignment can influence the magnitude of masking (DeAngelis et al., 1992). To determine whether the test orientation impacts the degree of suppression, we computed MI under conditions where the test stimulus was 45 degrees from the preferred orientation (the mask was also rotated by 45 degrees and remained orthogonal to the test stimulus). Under these conditions, responses to plaids exhibit significantly less suppression than when tested with the preferred stimulus (MI dF/F: −0.15 ± 0.02; n = 526; Wilcoxon rank sum test: p = 4.1e-69; Figures S1D and S1E).

One possible explanation for this relationship between masking and stimulus preference could be that neurons' responses to the preferred stimulus are close to their peak firing rates and therefore cannot exhibit facilitation due to a limited dynamic range. To investigate this, we compared the MI evoked by plaids composed of gratings at lower contrast. While decreasing the contrast significantly reduces the visually driven response (32% versus 48% contrast – membrane potential: p = 2.6e-4; spike rate: p = 2.1e-4; calcium imaging: p = 5.0e-4), the mean MI does not depend on the contrast of the component gratings (membrane potential: p = 0.58; spike rate: p = 0.73; calcium imaging: p = 0.88). This argues that a limited dynamic range does not explain our data.

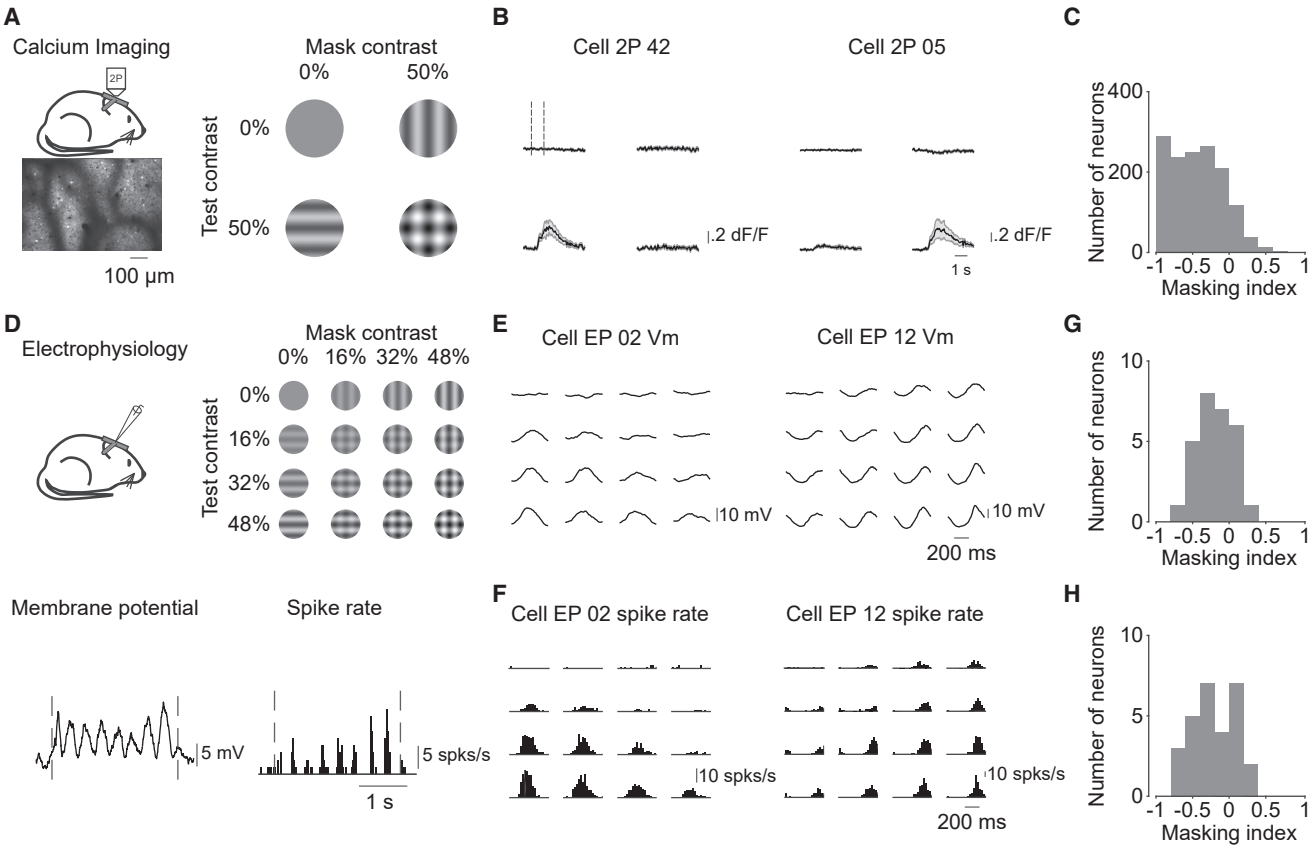

Figure 1. Responses to plaids are diverse in the mouse primary visual cortex (V1)

(A) Left: schematic of imaging setup (top) and example field of view (bottom). Right: stimulus set.

(B) Trial average dF/F responses to gratings and plaids for two example neurons. Shaded error bars represent standard error of the mean across trials. Dashed vertical lines represent time of stimulus presentation.

(C) Distribution of masking index for all cells at their preferred direction.

(D) Top: schematic of electrophysiology setup (left) and stimulus set (right). Bottom: trial average responses to a drifting grating for an example neuron for membrane potential (left) and spike rate (right).

(E) Cycle average membrane potential responses to gratings and plaids for two example neurons.

(F) Same as (E) for spike rate.

(G and H) Same as (C) for membrane potential (G) and spike rate (H).

See also Figure S1.

Cortex is not required for masking effects

Two differing mechanistic models have been proposed to account for the effects of masking, the cortical and feedforward models. The cortical model posits that cross-orientation suppression emerges from interactions between distinct populations of orientation tuned cortical neurons (Figure 2A). We sought to examine the role of recurrent cortical circuits for both cross-orientation suppression and facilitation by manipulating cortical activity.

We performed two manipulations to weaken the intracortical circuitry. First, we used long-term sensory adaptation to functionally lesion cortical activity (Figure 2B). Adaptation by prolonged exposure has the effect of reducing responses in V1 while leaving responses in the lateral geniculate nucleus of the thalamus (LGN) largely intact (Sanchez-Vives et al., 2000, King et al., 2016). If the effects of masking are invariant to adaptation of one of the component gratings, a cortical mechanism is unlikely (Freeman et al., 2002).

The effects of adaptation on masking were tested in interleaved blocks of adaptation and control trials. In each adaptation block, the mask stimulus (a vertical grating) was initially presented for 120 s, and then the mask, test (a horizontal grating), and plaid were randomly interleaved between 5-s "top-up" adaptation epochs (Figures 2B and 2C). Control blocks had the same temporal structure, but without stimulus presentation during the adaptation periods. To quantify the effects of adaptation to the mask stimulus on responses to gratings alone, neurons were grouped into two categories based on their responses to gratings: mask preferring and test preferring. In neurons that prefer the mask, sensory adaptation strongly reduces responses to the mask (control dF/F: 0.37 ± 0.03; adapt dF/F: 0.01 ± 0.004; n = 171 cells, 5 mice; two-way ANOVA, main effect of adaptation:

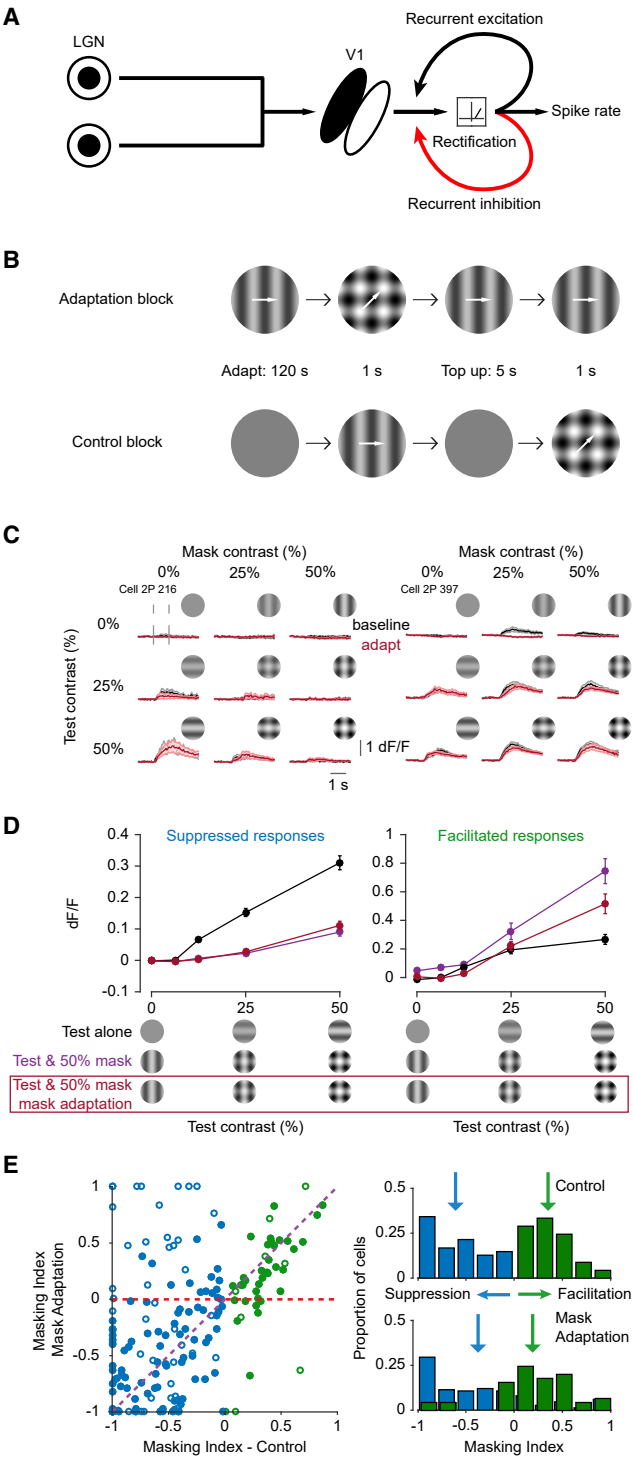

Figure 2. Effects of masking are robust to sensory adaptation

(A) Diagram depicting a circuit for a cortical mechanism of cross-orientation suppression.

(B) Schematic of stimuli for adaptation paradigm (top) and control (bottom).

(C) Example dF/F for two neurons before (black) and after (red) adaptation. Shaded error bars are standard error of the mean across trials.

(D) Average dF/F for test-preferring neurons in response to the test alone (black), test and 50% contrast mask (purple), and test and 50% contrast mask after adaptation (red) for neurons that were suppressed (MI < 0; left) or facilitated (MI > 0; right) by the mask before adaptation. Error bars are standard error of the mean across cells.

(E) Left: scatterplot comparing the masking index of all test-preferring neurons before (x axis) and after (y axis) adaptation. Color identifies neurons that were suppressed (blue) or facilitated (green) by the mask before adaptation. Filled symbols identify neurons that were significantly suppressed or facilitated before adaptation (unpaired t test: $p < 0.05$). Red dashed line indicates prediction of a cortical model, where adaptation should make the masking index zero. Purple dashed line indicates prediction of a non-cortical model, where there is no difference between control and adaptation conditions. Right: histograms comparing the masking index before (top) and after (bottom) adaptation. Arrows indicate mean.

See also Figure S2.

p = 3.3e-76; Figure S2A). This effect does not, however, generalize to responses to the test in test-preferring neurons. Responses in these neurons are only slightly, but still significantly, reduced (control dF/F: 0.30 ± 0.02; adapt dF/F: 0.25 ± 0.02; n = 194 cells, 5 mice; two-way ANOVA, main effect of adaptation: p = 0.002; Figure S2B). A similar pattern is seen in the response to plaids after mask adaptation. Mask-preferring neurons have a large reduction in their responses to plaids following adaptation (control dF/F: 0.37 ± 0.03, adapt dF/F: 0.01 ± 0.01; two-way ANOVA, main effect of adaptation: p = 1.1e-25; Figure S2C), whereas a smaller but significant effect is seen among test-preferring neurons (control dF/F: 0.24 ± 0.3 adapt dF/F: 0.21 ± 0.02; two-way ANOVA, main effect of adaptation: p = 0.02; Figure S2D). Adaptation therefore has the effect of selectively reducing cortical responses to one of the two components of the plaid stimulus.

Given that cortical models of cross-orientation suppression depend on the degree to which the cortex responds, selectively weakening responses to the mask stimulus should reduce cross-orientation interactions. However, after adaptation, test-preferring neurons suppressed under control conditions generally remain suppressed, and those that facilitate remain facilitated (suppressed cells: highest contrast grating dF/F: 0.31 ± 0.02; control plaid: 0.09 ± 0.01; adapt plaid: 0.11 ± 0.01; n = 149 cells; two-way ANOVA, main effect of adaptation: p = 0.27; facilitated cells: grating dF/F: 0.27 ± 0.03; control plaid: 0.74 ± 0.09; adapt plaid: 0.52 ± 0.07; n = 45 cells; two-way ANOVA, main effect of adaptation: p = 0.0001; Figures 2C and 2D).

If cortical circuitry were responsible for the interactions between test and mask stimuli, then we expect that the MI would approach 0 following adaptation (Figure 2E, red line). In contrast, if non-cortical mechanisms are responsible for cross-orientation interactions, then the MI should not depend on adaptation (Figure 2E, purple line). We find that there is a strong correlation between the MI before and after adaptation (r = 0.51, n = 189 cells), especially among those cells that remain significantly responsive to the test grating after adaptation (r = 0.76, n = 130 cells). Across the sample population, adaptation results in significant changes in the degree of masking (suppressed cells: control MI, −0.61 ± 0.03; adapt MI, −0.37 ± 0.04; n = 145 cells; paired t test, p = 3.3e-6; facilitated cells: control MI, 0.35 ± 0.03; adapt MI, 0.19 ± 0.06; n = 44 cells; p = 0.003), though these effects are less pronounced for the cells that are responsive to the test after adaptation (suppressed cells: n = 95, p = 0.02; facilitated cells: n = 35, p = 0.006).

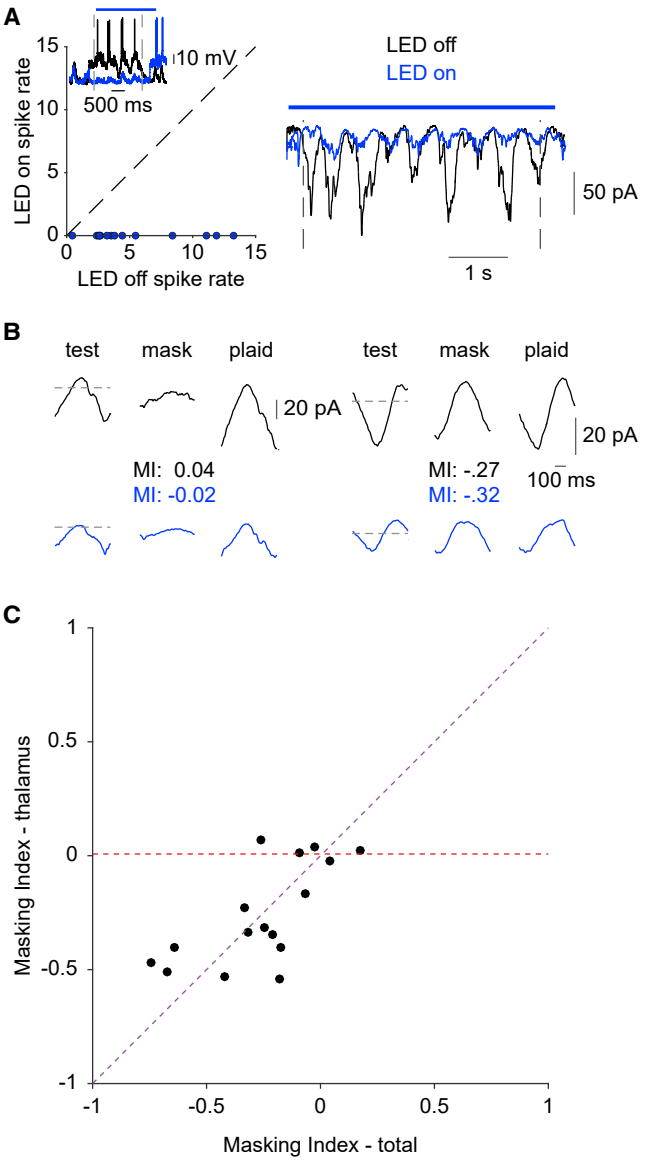

Figure 3. The effects of masking are reflected in the feedforward inputs to V1

(A) Left: scatterplot comparing spike rates elicited by a full-contrast grating with and without optogenetic stimulation. Inset shows and example current-clamp recording. Right: example voltage-clamp response to a grating in control (black) and during silencing (blue).

(B) Cycle averages of responses from two example neurons for the test, mask, and plaid in control (top) and during silencing (bottom). Dotted lines indicate baseline.

(C) Scatterplot comparing the masking index for all cells in control and during silencing. Red dashed line indicates prediction of cortical model where silencing should make the masking index zero. Purple dashed line indicates prediction of a non-cortical model where there is no difference between control and silencing conditions.

See also Figure S3.

Despite this regression of the MI toward zero, both facilitated and suppressed populations nonetheless have MIs significantly different than zero after adaptation (Student's t test: facilitated, $p = 0.003$; suppressed, $p = 6.2e\text{-}13$). Thus, while we find dramatic effects of adaptation on cortical responses to the mask, there are comparatively subtle effects on cross-orientation interactions, consistent with a feedforward contribution to this phenomenon.

Although our adaptation paradigm drives a large suppression of the mask representation, it is likely that there are nonspecific effects either on cortical or thalamic activity that may impact the interpretation of our results (King et al., 2016). We therefore sought to directly probe the relative contribution of thalamic and cortical circuits to masking by performing whole-cell recordings in layer 4 neurons while optogenetically silencing V1. Optogenetic stimulation of inhibitory PV^+ interneurons results in robust suppression of cortical pyramidal neurons (Figure 3A; Choi and Priebe, 2020; Cohen-Kashi Malina et al., 2016; Gu and Cang, 2016; Li et al., 2013; Lien and Scanziani, 2013). We held neurons at −70 mV using voltage clamp during optogenetic stimulation and measured the inward currents reflecting the isolated feedforward thalamic input (Figure 3B; n = 16 neurons).

Optogenetic suppression of visual cortex reduces visually evoked currents across the dataset (Figure 3B; geometric mean reduction in F1 = 0.63 ± 0.09; $p = 0.002$). Nonetheless, the amplitude of the isolated thalamic currents is still modulated by the presence of a mask (Figure 3B). The mask modulates the response in the same direction (i.e., suppression versus facilitation) for conditions in which the cortex is active or silenced in all but one neuron (11/12 neurons, neurons with MI between −0.1 and 0.1 excluded; Figure 3C). The magnitude of the response modulation is highly correlated between isolated thalamic and intact cortical circuits ($r = 0.67$), and there is no significant difference between the average modulation indexes (MI_{tot}: −0.22 ± 0.06, MI_{thal}: −0.23 ± 0.05; paired t test: $p = 0.88$). There are similarly no significant differences between the MI of the membrane potential records (Figure 1G) and both the isolated (unpaired t test: $p = 0.82$) and intact ($p = 0.65$) voltage-clamp recordings. The presence of cross-orientation interactions in the isolated thalamic inputs, and their similarity when the cortex is intact, indicate that the seed for cross-orientation interactions lay not in the cortex but in subcortical structures.

How might the recurrent cortical circuitry retain the effects of masking? It is possible that given the heterogeneous effects of masking in cortex, these effects are averaged out, resulting in only a small amount of modulation. Alternatively, the recurrent connectivity may be specific, resulting in a match between the effect of the mask in the feedforward and cortical input. We estimated the cortical input to V1 neurons by subtracting the isolated thalamic currents from the total measured current (Figure S3A; Lien and Scanziani, 2013). The mean MI of the cortical component (MI_{ctx}: −0.27 ± 0.06) does not differ significantly from the thalamic component (paired t test, $p = 0.88$) and MI_{ctx} is positively correlated with MI_{thal} ($r = 0.32$; Figure S3B). Notably, this correlation is somewhat weaker than the correlation between MI_{thal} and MI_{tot}, suggesting that while recurrent cortical circuitry does include some specificity, it does not retain the degree of precision present in the feedforward inputs.

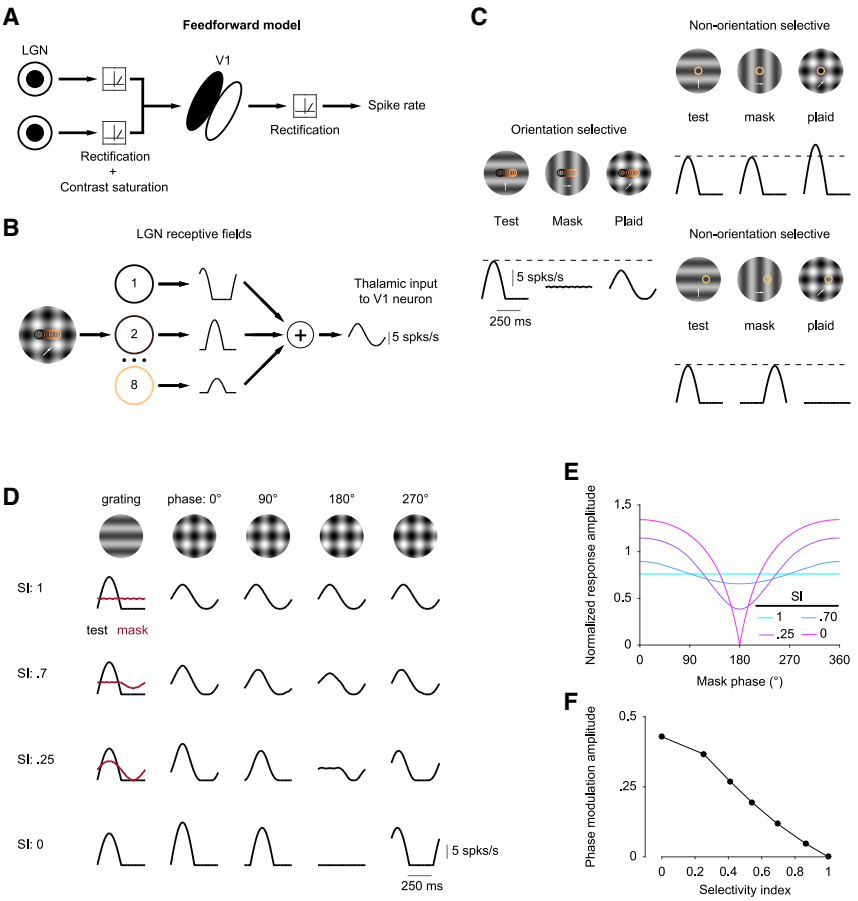

Figure 4. A feedforward model accounts for responses to plaids

(A) Diagram depicting a circuit for a feedforward mechanism of cross-orientation suppression.

(B) Framework for the implementation of the feedforward model. Each circle represents the receptive field of an individual thalamic afferent. Traces reflect responses of the afferents to one stimulus cycle.

(C) Model responses to the test, mask, and plaid for an orientation-selective (left) and two nonselective (right) model neurons with different receptive field positions (yellow circle). Dashed lines indicate the response amplitude of the test stimulus.

(D) Model neuron responses to test (black, first column), mask (red, first column), and plaids at multiple stimulus phases (columns 2–5). Each row corresponds to a different selectivity for the test and mask as measured by the selectivity index (SI).

(E) Response amplitude to the plaid stimulus as a function of stimulus phases for cells with varying SI. Responses are normalized to the amplitude of the test stimulus.

(F) Phase modulation amplitude as a function of SI for model neurons.

See also Figure S4.

A feedforward model predicts consequences of masking

Given the limited role of cortical circuits suggested by our experiments, we sought to determine whether a feedforward model could be sufficient to explain the diversity of masking effects observed in V1. In the feedforward model, suppressive interactions stem from nonlinearities (i.e., contrast saturation and rectification) in the thalamic input to the visual cortex (Figure 4A). This model has proven successful in explaining cross-orientation suppression in cat V1 (Priebe and Ferster, 2006; Li et al., 2006). It is not clear, however, whether a feedforward model can reproduce the facilitated responses seen in the mouse.

In the feedforward model, input from thalamic responses to grating and plaid stimuli are generated based on measured contrast and rectification nonlinearities (Priebe and Ferster, 2006). Thalamic relay cells with spatially offset receptive fields converge onto cortical neurons as a basis for their orientation selectivity (Hubel and Wiesel, 1962). This precise organization leads to thalamic responses that are temporally aligned when a preferred orientation grating is presented, resulting in a large modulation of the aggregate input, which is analogous to membrane potential (Figure 4B).

Mouse V1 neurons, however, exhibit a broad range of orientation selectivities (Niell and Stryker, 2008; Tan et al., 2011; Scholl et al., 2013). Many neurons are only weakly orientation tuned, lacking a precise alignment of their thalamic afferents. In some neurons, the response to the orthogonal gratings may be nearly as large as the response to the preferred orientation (Jia et al., 2010). It has been demonstrated that the effect of the mask is related to orientation selectivity, with strongly tuned neurons exhibiting suppression (Tring and Ringach, 2018; Guan et al., 2020). We therefore constructed a feedforward model in which the degree of orientation selectivity was adjusted by systematically controlling the spatial offset of thalamic afferents. When selectivity is altered in this manner, the predicted aggregate thalamic response to a plaid stimulus varied, showing either suppression or facilitation relative to the response to a single grating (Figure 4C).

Notably, we find that this simple model predicts that responses of weakly tuned neurons to plaids are sensitive to the precise location of their receptive field relative to the stimulus (Figure 4C, right panel). For example, if the receptive fields of thalamic neurons are positioned at plaid locations where large excursions of luminance occur (Figure 4C, top right), then model neurons exhibit large responses. If, on the other hand, the receptive fields are positioned at a location for which the mask reduces luminance modulations (Figure 4C, bottom right), then model neurons exhibit little, if any, response. By comparison, orientation-selective model neurons average across all of these regions, and therefore, changing the receptive field positions of these cells results only in timing changes.

To explore this interaction between receptive field location and orientation selectivity on the effect of masking, we systematically varied two model features, the degree of stimulus selectivity and the spatial phase of the mask grating (Figure 4D). As receptive field locations are fixed, shifting the spatial phase of

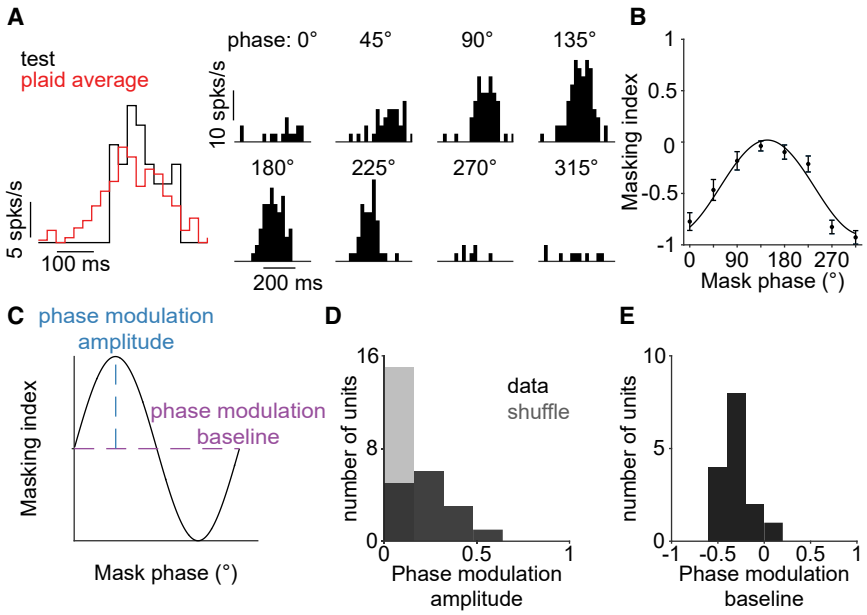

Figure 5. The effects of masking in the lateral geniculate nucleus

(A) Cycle-average spike rates of example single-unit LGN recording. Responses shown for test and plaid stimuli. Red trace indicates response average across plaid phases.

(B) Masking index for the cell in (A) at eight stimulus phases. Line is a sine-wave fit. Error bars are standard error (see STAR Methods).

(C) Diagram depicting the phase modulation amplitude and baseline of the sine fit.

(D) Histogram of LGN phase modulation amplitude. Light gray bins are shuffled controls.

(E) Histogram of LGN phase modulation baseline.

the mask effectively alters the relative positions of the luminance excursions and receptive field. We quantified the degree of selectivity of model neurons by computing the selectivity index (SI):

$$Selectivity\ Index = \frac{Test - Mask}{Test + Mask}$$

Altering the spatial phase of the mask stimulus has little impact on evoked responses of highly selective neurons: all mask spatial phases resulted in suppression. However, as SI declines, the mask spatial phase alters both the amplitude and timing of plaid responses. These modulations are systematic, with the largest facilitation occurring when the component gratings evoked responses that are spatially, and therefore temporally, in phase (Figure 4E). The sensitivity of each cell to the mask spatial phase is summarized by its spatial phase modulation amplitude. Notably, the model predicts a strong inverse relationship between modulation amplitude and stimulus selectivity (Figure 4F).

Our model uses a precise alignment of thalamic inputs to generate phase-sensitive responses to plaids (Hubel and Wiesel, 1962). There is, however, evidence suggesting that connectivity in mouse V1 may use alternative receptive field alignments (Liu et al., 2010; Lien and Scanziani, 2013; Pattadkal et al., 2018). To see how alternative receptive field alignments affect model cell phase sensitivity, we generated a population of model neurons with randomly distributed thalamic receptive field locations (see STAR Methods). Even with random connectivity, mask phase selectivity is present and exhibits the same relationship with SI seen in the organized model ($r = -0.87$, Figure S4), indicating that the interaction between selectivity and mask phase sensitivity emerge from multiple feedforward input arrangements.

Thus, we recapitulate the observed diversity of masking effects seen in V1 with a simple, subunit-based feedforward model. Moreover, this model makes specific predictions about how the diversity of masking should depend on stimulus phase and neuron selectivity.

Phase sensitivity in the feedforward inputs to V1

Our feedforward model predicts that the mask phase should impact the amplitude and timing of visual responses in individual LGN relay cells and the aggregate input to V1 neurons. To demonstrate the validity of this model, we measured the sensitivity to mask spatial phase in the feedforward input to V1 by recording extracellular single-unit activity in the LGN (n = 15 units). Changes in mask spatial phase lead to systematic shifts in both the timing (one-way ANOVA, main effect of response phase $p < 0.05$ for 13/15 neurons) and amplitude (one-way ANOVA, main effect of amplitude $p < 0.05$ for 14/15 neurons) of thalamic responses as predicted by our simple model (Figures 5A and 5B). To estimate the average response to the plaid across mask phases, we computed the mean of the plaid responses for each unit across all eight spatial phases (Figure 5A, red trace). The average plaid across our dataset yields a suppressed response compared to the test stimulus ($F1_{plaid\ \ average}/F1_{test}$, geometric mean = 0.79 ± 0.1).

We further quantified the phase dependence of the LGN responses by fitting the MI computed at each spatial phase with a sinusoid to determine the amplitude of the modulation across phases (Figure 5B). The amplitude of this fit indicates the phase sensitivity (phase modulation amplitude), while the baseline indicates the average effect of the mask across phases (Figure 5C). Thalamic responses exhibit significantly greater phase modulation amplitude than shuffled controls (Figure 5D; median phase modulation amplitude: 0.23 ± 0.04 bootstrap method; shuffle: 0.0004 ± 0.00001; Wilcoxon signed rank: $p < 0.001$). Although responses could be either facilitated or suppressed in response to individual plaids, the average effect of the mask is suppression (Figure 5E; mean phase modulation baseline: −0.33 ± 0.04).

While we observe sensitivity to mask phase in individual LGN neurons, this sensitivity could decline in the aggregate relay cell input to cortical neurons. To isolate the aggregate thalamic input, we performed voltage-clamp recordings from L4 neurons in V1 under optogenetic stimulation of PV+ cells while varying the mask spatial phase (n = 6 cells). Isolated thalamic feedforward

inputs are sensitive to stimulus phase (Figure 6A; $F1_{thal}$, median phase modulation amplitude: 0.26 ± 0.04, bootstrap method) and are somewhat larger than the control condition ($F1_{tot}$, median phase modulation amplitude: 0.19 ± 0.06), but this effect is not significant (Wilcoxon signed rank: p = 0.06). The estimated cortical contribution is similarly modulated by phase as the intact response ($F1_{tot} - F1_{thal}$, median phase modulation amplitude: 0.19 ± 0.05). Thus, we find the phase-dependent signals predicted by our feedforward model in the LGN and the aggregate thalamic input to V1.

Spatial phase modulates the effect of masking in V1

Our initial measurements of masking revealed diverse responses across the population but were based on a single spatial configuration of test and mask (Figure 1). The diversity of responses could emerge if the mask spatial phase plays a role in whether neurons are suppressed or enhanced to the plaid stimulus. To test whether the phase-dependent input to the cortex can explain the diversity of masking effects seen in the cortex, we measured responses of V1 neurons to plaids at multiple spatial phases. Similar to our observations in the LGN, varying the stimulus phase leads to dramatic shifts in the neuronal response amplitude to plaids, often shifting between suppression and facilitation in a single neuron (Figures 6B and 6C, left panel). Across our electrophysiological and imaging datasets, we find that the spatial phase of the mask stimulus elicits large, significant changes that follow the expectations of the feedforward model. In our electrophysiological records, 65% (13/20 cells, by membrane potential) of neurons are significantly modulated by stimulus phase (one-way ANOVA: $p < 0.05$). A similar proportion of neurons are significantly modulated by phase in our calcium imaging dataset (57%, 468/814 cells, 11 mice; Figure 6E). Overall, the phase modulation amplitude is significantly greater than shuffled controls for membrane potential (median phase modulation amplitude: 0.21, shuffle: 0.006; Wilcoxon signed rank: $p < 0.001$), spike rate (median phase modulation e amplitude: 0.22, shuffle: 0.002; $p < 0.001$), and dF/F (median phase modulation amplitude: 0.19, shuffle: 0.08; $p < 0.001$). As a measure of the overall effect of masking, we also quantified the baseline of the sine wave fit. The phase modulation baseline is negative on average (membrane potential: −0.26 ± 0.04; spike rate: −0.31 ± 0.07; dF/F: −0.31 ± 0.01 for dF/F), indicating that neurons are more likely to be suppressed by the plaid across phases (Figure 6F). Altogether, this reveals a strong dependence of stimulus phase in the effect of masking, consistent with the feedforward, but not the cortical, model.

Our feedforward model applies to simple cells, but complex cells also exhibit effects of masking. Because complex cells integrate responses from multiple simple cells, our expectation is that this integration should make these cells less sensitive to the mask spatial phase. In our electrophysiology dataset, we find that the modulation ratio (F1/F0), a metric for phase sensitivity at the drift rate of the grating, is correlated with the degree of phase modulation both for membrane potential (r = 0.4) and spike rate (r = 0.46). Consistent with this finding, average phase modulation amplitude is lower in complex cells (F1/F0 <1, by spike rate; mean phase modulation amplitude: 0.08 ± 0.02) than in simple cells (F1/F0 >1; mean phase modulation amplitude: 0.28 ± 0.5). The phase modulation baseline, which reflects the overall effects of masking, is similar between simple (mean phase modulation baseline = −0.27 ± 0.08) and complex cells (mean phase modulation baseline = −0.35 ± 0.16) and is not correlated with the F1/F0 (membrane potential: r = −0.02; spike rate: r = 0.008). These results are consistent with a model in which masking in simple cells is phase sensitive, while complex cells inherit masking but, due to integration across multiple simple cells, are less sensitive to mask spatial phase.

What determines when a given stimulus phase will elicit a large or small response? In the model, the receptive fields are fixed at a particular point in the plaid. This generates the maximum response when the two component gratings are aligned in phase. In our recordings, we do not have access to the location of the individual LGN receptive fields. Therefore, the plaid phase that elicits the maximum response is uniformly distributed (Figure 6D).

Whereas the preferred mask phase is uniformly distributed, the feedforward model predicts that the phases at which suppression and enhancement occur depend on the timing of the responses to the test and mask alone. Specifically, there should be enhancement when those responses are temporally aligned and suppression when they are out of phase (Figures 4D and 4E). To test whether this linear combination of the test and mask can account for the amplitude and timing of responses to the plaid, we summed the membrane potential responses to the test and mask alone and after shifting the timing of the mask response in accordance with the expected change in phase (Figure 6B, gray dashed lines). This linear computation is highly predictive of both amplitude (r = 0.82) and timing (r = 0.53) of the response to the plaid (Figure 6G). Thus, the phase dependence of masking is directly predicted by the linear summation of LGN inputs in V1 neurons.

The feedforward model predicts that mask phase sensitivity emerges in response to changes in the spatial arrangement of luminance excursions that occur with different phase relationships between the test and mask. However, if the mask drifts at a higher frequency than the test, this will disrupt this fixed spatial arrangement, and the resulting plaid will cycle through multiple spatial phase relationships in time. Our model predicts that this will result in responses that are modulated by spatial phase at the drift rate of the mask but that there should be no dependence on phase at the drift rate of the test (Figures S5A and S5B). In extracellular recordings in the LGN, we find low phase sensitivities (< 0.1) with a 2-Hz test and a 10-Hz mask (Figures S5C and S5D). In a larger population collected with calcium imaging, we confirm that the phase modulation amplitude is significantly lower with a high-frequency mask (n = 255 cells, 2 mice; paired t test: p = 1.2e-18; Figures S5E–S5G). The thalamic inputs and cortical responses preserve cross-orientation interactions when the mask drift rate is high, but the mask phase modulations occur within a single test cycle.

Spatial phase modulation depends on stimulus selectivity

In addition to predicting that masking will be sensitive to the stimulus phase, the feedforward model predicts a nearly linear relationship between SI and phase modulation amplitude

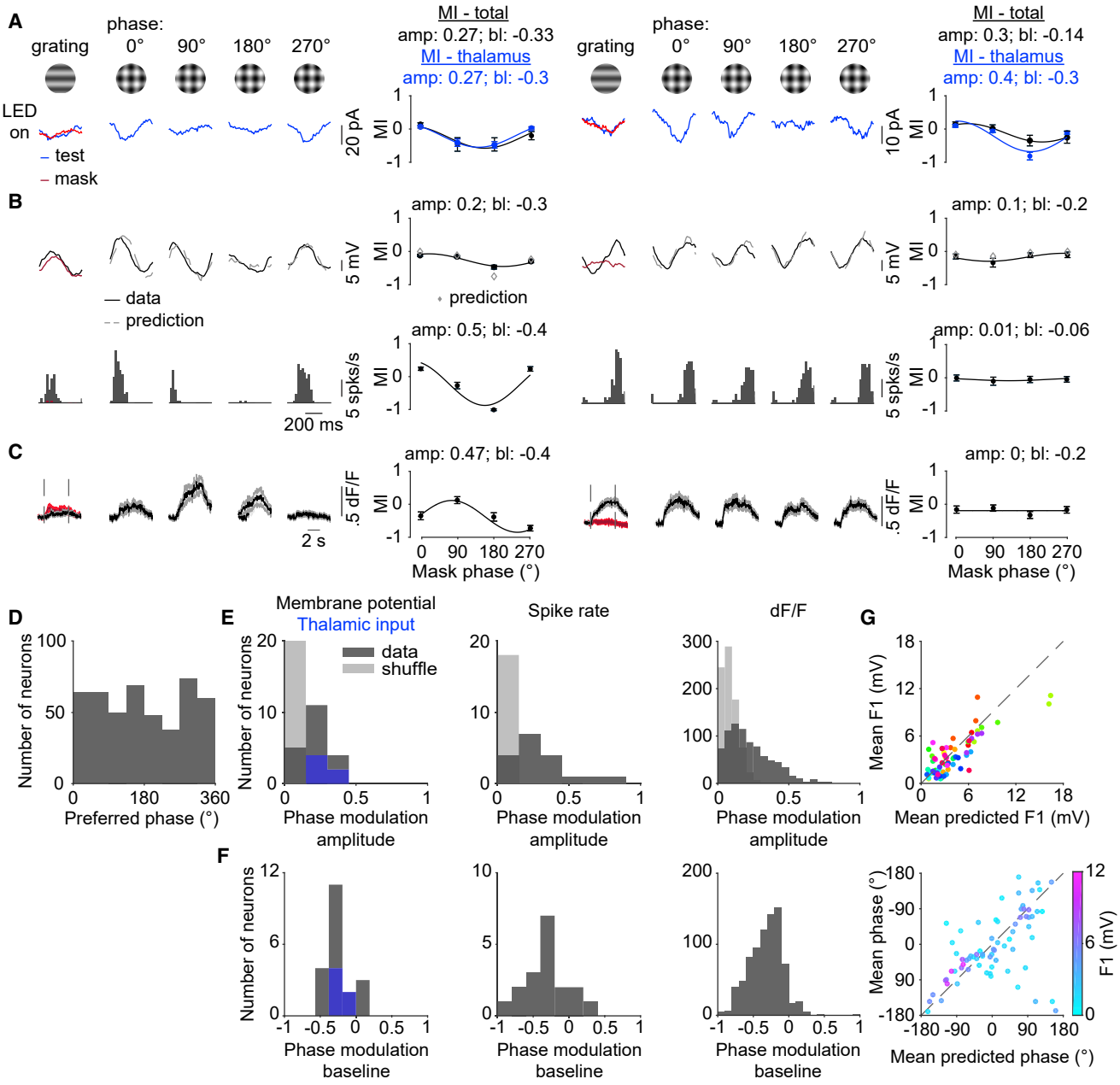

Figure 6. V1 Responses to plaids are phase-sensitive

(A) Cycle average voltage-clamp recordings during optogenetic activation of PV+ cells in response to gratings and plaids at four stimulus phases for two example neurons. Plots depict dependence of masking index on mask spatial phases for MI_{tot} (black) and MI_{thal} (blue). Error bars are standard error. Data are fit with a sinusoid (amp, amplitude; bl, baseline).

(B) Cycle-average membrane potential (top) and spike rate responses (bottom) to test (black), mask (red) and plaids at four stimulus phases for two example neurons. Gray dashed lines indicate a linear prediction based on the response to the test and mask alone. Plots depict the dependence of masking index on mask phase. Error bars are standard error. Gray dots illustrate linear prediction.

(C) Same as (B) for dF/F. Error bars are standard error of the mean across trials.

(D) Histogram of the preferred stimulus phase in the imaging dataset.

(E) Histograms showing the phase modulation amplitudes for membrane potential and (left), spike rate (center), and dF/F (right). Light bins depict a shuffled control. Blue bins depict the isolated thalamic input.

(F) Same as (E) but for phase modulation baseline.

(G) Scatterplots comparing the amplitude (top) and phase (bottom) of the linear prediction (x axis) and membrane potential response (y axis) to plaids across phases. Four responses are plotted per neuron to represent the response to each stimulus phase. In the top panel, color code is by neuron; in the bottom panel, color code is by F1 modulation amplitude.

See also Figure S5.

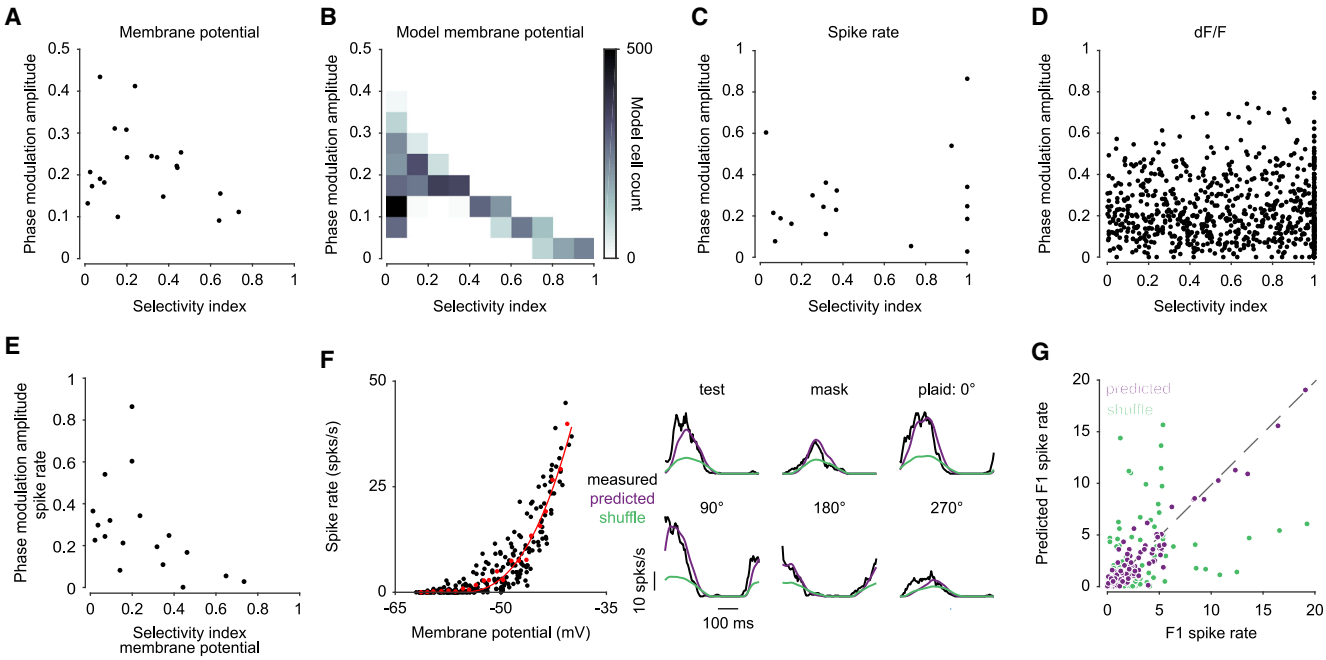

Figure 7. Phase sensitivity depends on the selectivity of membrane potential responses to the test and mask

(A) Scatterplot comparing the SI (x axis) and phase modulation amplitude (y axis) of membrane potential responses.

(B) Heatmap comparing SI and phase modulation amplitude for a simulated population of model neurons sampling at only four phases.

(C) Same as (A) for spike rate.

(D) Same as (A) and (C) for dF/F.

(E) Scatterplot comparing membrane potential SI to spike rate phase modulation amplitude.

(F) Left: estimate of threshold nonlinearity for an example neuron. Right: spike rate responses to gratings and plaids for measured spike rate (black), spike rate prediction from the threshold fit (purple), and a shuffled control using a different cell's threshold nonlinearity (green).

(G) Scatterplot comparing measured response amplitudes (x axis) with those predicted from the cell's own threshold non-linearity (purple) or another cell's thresold non-linearity (green).

See also Figures S6 and S7.

(Figure 4F). Upon initial inspection, however, the membrane potential responses only partially follow this pattern (Figure 7A). Neurons with high selectivity indices exhibit membrane potential responses that conform to the predicted relationship, with a nearly linear pattern of decreasing phase modulation amplitude as selectivity increases. Neurons with low selectivity, however, exhibit both low and high phase modulation amplitudes, contrary to the expectations of the feedforward model.

What can account for this apparent contradiction between the model and data? One difference between the data and model concerns the number of stimulus phases used to measure phase modulation amplitude. Model neuron responses were measured at 360 stimulus phases. Due to experimental constraints, membrane potential data for most neurons were gathered at only four stimulus phases. Thus, we hypothesized that the under-sampling of stimulus phase in our dataset might result in an underestimate of phase modulation by missing points that reflect the peak or trough of the function.

To determine whether our experimental under-sampling of the full phase tuning curve might be biasing our measurements, we restricted our model to only sample the limited set of phases explored in the experiment. Under these conditions, the model predicts a linear relationship at higher SIs and a scattering of phase modulation amplitude values at lower SIs, matching the experimental data (Figure 7B).

While plaid phase sensitivity and selectivity are strongly linked at the membrane potential level, there is no clear relationship at the spiking level across the population of the same neurons (Figure 7C) or in our calcium imaging dataset (Figure 7D). We do find that the SI of the membrane potential is related to the phase modulation amplitude of the spike rate ($r = -0.48$; Figure 7E). Thus, we hypothesized that this discrepancy lies in the nonlinearities (and the variation of these nonlinearities across neurons) that define how membrane potential is converted to spikes (Priebe et al., 2004). To test whether such variation in nonlinearity disrupts the relationship between SI and phase modulation amplitude, we passed model responses through a rectifying nonlinearity that varies in threshold. This variation in threshold captures the weak relationship between spike rate SI and phase modulation amplitude seen in the data (Figure S6B). Thus, we propose that variation in the nonlinearity across the population reorganizes their relative selectivity indices, obscuring the relationship with phase modulation amplitude across the sample population.

To determine whether there is such variation in thresholds in our dataset, we generated spike rate predictions from the membrane potential response by fitting the nonlinearity (Figure 7F).

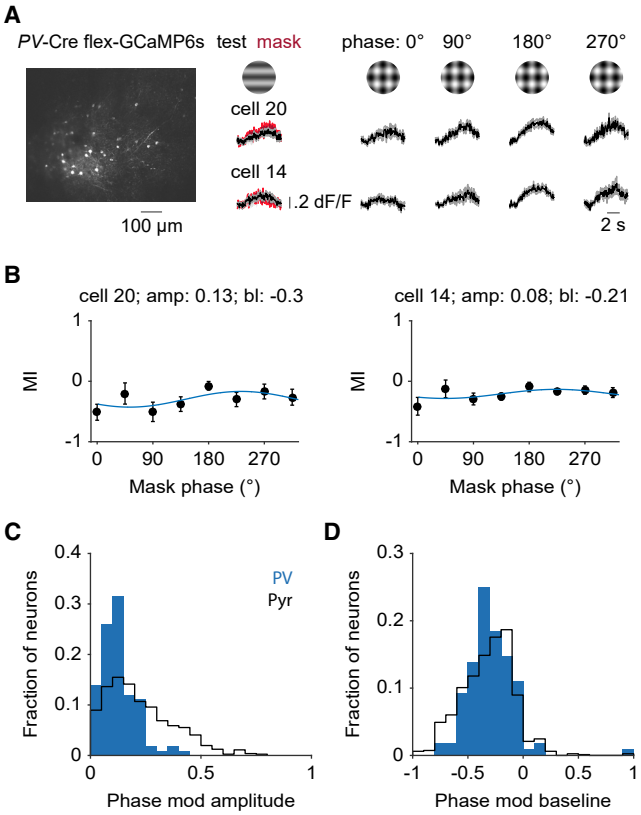

Figure 8. Limited phase sensitivity in inhibitory PV$^+$ neurons

(A) Left: example field of view of a PV-Cre mouse injected with flex-GCaMP6s. Right: example responses of two PV$^+$ neurons to gratings and plaids at multiple stimulus phases. Shaded error bars are standard error of the mean across trials.

(B) Plots depicting the masking index of the two example neurons in (A) at eight stimulus phases. Data (black) are fit with sinusoids (blue) to measure the baseline and amplitude of the modulation. Error bars represent standard error of the mean across trials.

(C) Histogram showing distributions of phase modulation amplitude for PV$^+$ (filled, blue) and excitatory (outline, black; same data as shown in Figure 6F) neurons.

(D) Same as (C) for phase modulation baseline.

Using this approach, we can reliably predict the spiking of each neuron from its subthreshold response. Across the population, there is a strong correlation in the measured and predicted spike rates (r = 0.95; Figure 7G), phase modulation amplitude (r = 0.96), and the SI (r = 0.7). These transformations are therefore predictable at the level of individual neurons. To see how the diversity of the threshold nonlinearities may obscure this relationship at the population level, we generated spike rate predictions for each neuron with the nonlinearity fit of a different neuron in the dataset. These shuffled controls are considerably worse at accounting for the firing rate in response to gratings and plaids (r = 0.31, Figures 7F and 7G) and the associated phase modulation amplitude (r = 0.22) and SI (r = 0.14). These findings highlight how an intervening nonlinearity, like spike threshold, can obscure a strong relationship between parameters at the membrane potential level.

In contrast to phase modulation amplitude, phase modulation baseline exhibits a slight positive correlation with membrane potential SI (r = 0.3; Figures S6C and S6D). This relationship is also altered by threshold, as SI and phase modulation baseline exhibit a small negative correlation in both spike rate (r = −0.24; Figure S6C) and calcium imaging (r = −0.2; Figures S7A and S7B). Taken together, these results suggest that as selectivity increases, the amplitude of the membrane potential phase modulation curve decreases while the mean of the curve shifts upward, resulting in a neuronal response that is less sensitive to phase and on average less modulated by the mask. These dependencies emerge from a simple feedforward model that includes contrast saturation and response rectification.

Cross-orientation interactions manifest differently in PV$^+$ interneurons and pyramidal cells

The suppressive and facilitative effects of mask stimulation emerge naturally in a feedforward model, but V1 neurons also receive extensive intracortical inhibitory inputs that may play a role in this process. We therefore sought to examine the impact of plaid stimulation on a prominent subtype of cortical interneuron, PV$^+$ neurons. PV$^+$ interneurons are broadly selective, and their activation linearly suppresses pyramidal cell firing, implicating them in normalization processes such as cross-orientation suppression (Sohya et al., 2007; Niell and Stryker, 2008; Kerlin et al., 2010; Ma et al., 2010; Runyan et al., 2010; Hofer et al., 2011; Atallah et al., 2012; Wilson et al., 2012). PV$^+$ interneurons were selectively labeled using Pvalb-IRES-Cre mice injected with flex-GCaMP6s, and we used two-photon calcium imaging to measure responses to gratings and plaids at multiple spatial phases (Figures 8A and 8B). We then compared these measurements to responses obtained from the population of genetically identified pyramidal neurons described in Figures 6 and 7. Our expectations were that if PV$^+$ cells contribute to the overall suppression of pyramidal cells, then plaid stimuli should provide weaker suppression (as predicted by the supralinear stabilized network [SSN] model; Ozeki et al., 2009; Rubin et al., 2015; Ahmadian et al., 2013) or even facilitation (as predicted by the normalization model; Heeger, 1992). Further, if PV$^+$ cells are responsible for the phase-dependent modulation of pyramidal cells, then their suppression should be as modulated as pyramidal cells.

Consistent with the literature, PV$^+$ cells are significantly less selective than pyramidal cells, whether quantified across orientations (mean orientation selectivity index [OSI]: PV: 0.39 ± 0.03, n = 108 cells, 5 mice; Pyr: 0.75 ± 0.01, n = 281 cells, 7 mice; p = 2.88e-21, Mann-Whitney *U* test) or by the selectivity for the test and mask gratings (SI: PV: 0.30 ± 0.02, n = 108 cells, 5 mice; Pyr: 0.61 ± 0.01, n = 814 cells, 11 mice; p = 9.56e-19). We measured the effects of masking at multiple mask spatial phases to extract both how the specific geometry of the visual stimulus modulates inhibitory cell responses in addition to the baseline degree of masking (Figure 8B). Whereas mask phase has a profound impact on pyramidal cell responses, significantly fewer PV$^+$ cells are modulated by mask phase (22/108; p = 3.75e-13, chi-square test). Because response amplitude varies weakly across mask spatial phase, the MI exhibits only weak modulations (median amplitude: PV, 0.11; p = 3.81e-12, Mann-Whitney

U test; Figure 8C). In contrast, we find that pyramidal cells and PV^+ interneurons exhibit similar degrees of overall suppression across mask phases (mean baseline: PV, −0.28 ± 0.02; p = 0.46, Mann-Whitney *U* test; Figure 8D). The convergence of these results indicates that the PV^+ interneurons respond to distinct aspects of the visual plaid than their pyramidal cell counterparts. Further, PV^+ neurons do not exhibit responses that could account for the spatial-phase-dependent masking or have weaker suppression than pyramidal cells.

DISCUSSION

The feedforward model provides a simple mechanistic account of masking in V1. Both cross-orientation suppression and facilitation arise from the same feedforward mechanism, with response diversity accounted for by the broad range of orientation selectivities in mouse V1. We have demonstrated that the spatial phase of the plaid is a determining factor of response amplitude of V1 neurons with low selectivity between the test and mask stimulus. This phase sensitivity naturally emerges from the spatial structure of the afferent receptive field and does not rely on cortical interactions.

We utilized multiple experimental approaches to define a feedforward origin of masking. Although each of these experimental paradigms may have limitations (for example, optogenetic experiments may not result in complete suppression of feedback from higher visual areas), the strength of our approach lies in their collective interpretation. By reversibly lesioning V1 with both sensory adaptation and optogenetics, we have shown that there is no need to invoke a cortical mechanism to explain the effects of masking in mouse V1. Furthermore, we demonstrate that both the phase dependency and net suppressive effects of masking are present in both individual LGN neurons and the feedforward thalamic input to V1 neurons. This suggests that most of the nonlinearities associated with masking arise prior to the thalamocortical synapse, likely from rectification and contrast saturation in the retina and thalamus. Indeed, the cortical responses to plaids are accounted for by a subunit-based model, which includes these two nonlinearities in the cortical inputs. It is possible that additional nonlinearities, such as synaptic depression at the thalamocortical synapse, also play a role in shaping these responses (Carandini et al., 2002; Freeman et al., 2002). Our finding that LGN spiking matches cortical input, however, suggests that thalamocortical transformations have relatively little impact on masking. Further, synaptic depression is not believed to be strong enough to account for the degree of masking seen in cortex (Boudreau and Ferster, 2005; Reig et al., 2006) and, unlike our data, is sensitive to anesthesia (Reinhold et al., 2015). In addition to subcortical nonlinearities, the nonlinear transformation between input and spiking output in cortex also contributes by enhancing the phase dependence of masking, while the variability of this transformation alters the relationship between selectivity and masking observed across the cortical population.

These results point to two factors that determine the strength of neuronal response to plaid stimuli: (1) the selectivity of the V1 neuron for the test over the mask and (2) the relative position of the thalamic afferents and the luminance excursions of plaid stimuli (i.e., spatial phase). In light of this latter sensitivity to phase, which depends on the stimulus, but not on the cell, it does not seem appropriate to categorize V1 neurons as "plaid suppressed" or "plaid preferring" on the basis of a facilitated response to a plaid at one spatial configuration (Guan et al., 2020). Furthermore, experiments that measure responses to plaids in mouse V1 must consider the effect of spatial phase. For example, plaids have been used to measure selectivity to complex motion patterns in mouse V1 (Juavinett and Callaway, 2015; Muir et al., 2015, 2017; Palagina et al., 2017), and our data suggest that this selectivity will be phase sensitive. If anything, our dataset likely underestimates the degree of phase sensitivity across the population, as we employed a limited number of spatial phases that may not precisely identify the peak and trough of the phase interactions. It is likely that there are additional stimulus features not explored here, such as size, contrast, and spatial frequency, which also contribute to the degree and phase sensitivity of masking (DeAngelis et al., 1992; Tring and Ringach, 2018).

Our experiments were confined to mouse V1, but there is reason to believe that the findings presented here are applicable to other species. Previous research has demonstrated that in both cats and primates, feedforward mechanisms account for the effects of cross-orientation suppression in V1 (Priebe and Ferster, 2006; Li et al., 2006, Koelling et al., 2008, Freeman et al., 2002). Our finding that the MI (and its phase sensitivity) depends on the relative response to the test and the mask also resolves the reported discrepancies across species in the effects of masking. While the diversity of orientation tuning is largest in mouse V1, primate V1 does contain neurons with low orientation selectivity (Ringach et al., 2002; Tan et al., 2014), whereas neurons in cat V1 are uniformly sharply tuned (Scholl et al., 2013). Thus, this explains the frequency of observations of facilitation being highest in the mouse (Juavinett and Callaway, 2015; Muir et al., 2015, 2017; Palagina et al., 2017), present in the primate (Guan et al., 2020), and absent in the cat (DeAngelis et al., 1992, Priebe and Ferster 2006). Finally, our work resolves that the differences in the prevalence of facilitation and suppression across mouse studies lie in the definition of the test stimulus. When the test stimulus is defined as the preferred orientation, greater suppression is observed than when the test is defined as nonpreferred orientations.

In our model, lateral geniculate receptive fields were imagined as circularly symmetric, lacking orientation selectivity. Some mouse LGN neurons, however, have been shown to exhibit a limited degree of orientation selectivity (Piscopo et al., 2013; Scholl et al., 2013; Zhao et al., 2013; Suresh et al., 2016). It is possible that these orientation-selective LGN neurons respond in a way not accounted for by our simple model, although our thalamic records match the general response properties predicted by the model. Such elaborations suggest that some of the nonlinear interactions we have explored in the feedforward inputs may arise as early as the retina. In addition, our model is based on the integration of LGN inputs in cortical cells, typically thought to occur primarily in layer 4. However, we observed comparable effects of masking among electrophysiological records from layers 4 and 2/3 (and comparable results from calcium imaging from layer 2/3). This may reflect the promiscuous input from the LGN to both cortical layers (Ji et al., 2016; Kondo and Ohki, 2016). Alternatively, this may reflect precise

retinotopic connectivity where pre- and post-synaptic partners have aligned receptive fields subunits (Cossell et al., 2015). We found some evidence for this precise connectivity, as both the cortical and thalamic components in our optogenetic experiments were similarly modulated by mask spatial phase.

The feedforward account is distinct from circuit models such as the SSN model, which rely on intracortical inhibition to explain cross-orientation suppression (Rubin et al., 2015). Inhibitory interneurons, however, do not have a receptive field geometry that could render them sensitive to the relative phase of the test and the mask (Niell and Stryker, 2008; Ma et al., 2010; Liu et al., 2009). Our recordings from PV^+ interneurons reflect this difference in functional selectivity, as these neurons were significantly less modulated by the spatial phase of the mask than excitatory neurons. The behavior of PV^+ neurons may seem to be at odds with our feedforward model given that PV^+ neurons are weakly tuned for orientation (Niell and Stryker, 2008; Ma et al., 2010; Sohya et al., 2007; Kerlin et al., 2010; Atallah et al., 2012), and our model predicts an inverse relationship between orientation tuning and phase sensitivity. This discrepancy may lie in how PV^+ neuron responses emerge. Unlike pyramidal cells, PV^+ neurons integrate the responses of nearby neurons with distinct spatial receptive fields and orientation preferences, which would blur the impact of mask spatial phase (Bock et al., 2011; Hofer et al., 2011; Kerlin et al., 2010; Runyan et al., 2010; Runyan and Sur, 2013; Scholl et al., 2015). In support of this, pyramidal cells with complex receptive fields were also less sensitive to mask phase than simple cells. While PV^+ neurons may not provide the input necessary to account for the spatially specific modulations we describe here, they may nonetheless act as local stimulus energy sensors that provide a normalization signal for visual cortex. It is important to note, however, that the SSN model proposed that while both excitatory and inhibitory cells exhibit suppressive effects, the effects should be weaker in inhibitory cells than pyramidal cells (Rubin et al., 2015). We have found instead that the overall degree of suppression in PV^+ inhibitory cells matches that of pyramidal cells.

In contrast to circuit models, other cortical models offer a computational perspective on cross-orientation suppression. In the normalization model, for example, the two different stimulus orientations composing the plaid lead to the activation of a greater number of cortical neurons, resulting in increased suppression (Heeger, 1992). Although that circuit is not consistent with our proposed mechanism, the normalization model provides a compact description of many of the nonlinear response properties of cortical neurons and is a powerful conceptual model of cortical responses (Carandini and Heeger 2011). One interpretation of our results is that the normalization model provides general rules that govern cortical responses, and in the case of cross-orientation suppression, the feedforward circuit implements those rules.

One successful approach to understanding sensory processing is to focus on the computation being performed separate from the specific implementation (Marr, 1982; Marr and Poggio 1976). As shown here, however, neurons may respond in ways that are superficially misleading. For example, one might interpret cross-orientation facilitation as a unique computation, separate from that of cross-orientation suppression. By taking the alternate approach of focusing on the mechanistic details, we have revealed that cross-orientation interactions are a direct consequence of the spatial geometry and position of the plaid. Nonetheless, both the computational and mechanistic approaches, and the interactions between these approaches, are essential to understand sensory processes.

STAR★METHODS

Detailed methods are provided in the online version of this paper and include the following:

- KEY RESOURCES TABLE
- RESOURCE AVAILABILITY
  - Lead contact
  - Materials availability
  - Data and code availability
- EXPERIMENTAL MODEL AND SUBJECT DETAILS
  - Animals
- METHOD DETAILS
  - Electrophysiology
  - Imaging
  - Stimulus Presentation
- QUANTIFICATION AND STATISTICAL ANALYSIS
  - Electrophysiology
  - Imaging

SUPPLEMENTAL INFORMATION

Supplemental information can be found online at https://doi.org/10.1016/j.neuron.2021.10.017.

ACKNOWLEDGMENTS

We thank Grace Link for surgical assistance and both Hillel Adesnik and Uday Jagadisan for their valuable feedback on a previous version of the manuscript. This work was supported by grants from the National Eye Institute (R01-EY031328 to L.L.G. and R01-EY025102 to N.J.P.).

AUTHOR CONTRIBUTIONS

Conceptualization, D.B., N.J.P., and L.L.G.; methodology, D.B., N.J.P., and L.L.G.; investigation, D.B., N.J.P., and L.L.G.; formal analysis, D.B., N.J.P, and L.L.G.; writing – original draft, D.B.; writing – review & editing, D.B., N.J.P., and L.L.G.; funding acquisition, N.J.P. and L.L.G.

DECLARATION OF INTERESTS

The authors declare no competing interests.

Received: April 26, 2021
Revised: September 3, 2021
Accepted: October 12, 2021
Published: November 3, 2021

REFERENCES

Ahmadian, Y., Rubin, D.B., and Miller, K.D. (2013). Analysis of the stabilized supralinear network. Neural Comput. *25*, 1994–2037.

Alitto, H.J., and Dan, Y. (2010). Function of inhibition in visual cortical processing. Curr. Opin. Neurobiol. *20*, 340–346.

Atallah, B.V., Bruns, W., Carandini, M., and Scanziani, M. (2012). Parvalbumin-expressing interneurons linearly transform cortical responses to visual stimuli. Neuron *73*, 159–170.

Blakemore, C., and Tobin, E.A. (1972). Lateral inhibition between orientation detectors in the cat's visual cortex. Exp. Brain Res. *15*, 439–440.

Bock, D.D., Lee, W.C., Kerlin, A.M., Andermann, M.L., Hood, G., Wetzel, A.W., Yurgenson, S., Soucy, E.R., Kim, H.S., and Reid, R.C. (2011). Network anatomy and in vivo physiology of visual cortical neurons. Nature *471*, 177–182.

Bonds, A.B. (1989). Role of inhibition in the specification of orientation selectivity of cells in the cat striate cortex. Vis. Neurosci. *2*, 41–55.

Boudreau, C.E., and Ferster, D. (2005). Short-term depression in thalamocortical synapses of cat primary visual cortex. J. Neurosci. *25*, 7179–7190.

Brainard, D.H. (1997). The psychophysics toolbox. Spatial Vision *10*, 433–436.

Carandini, M., and Heeger, D.J. (1994). Summation and division by neurons in primate visual cortex. Science *264*, 1333–1336.

Carandini, M., and Heeger, D.J. (2011). Normalization as a canonical neural computation. Nat. Rev. Neurosci. *13*, 51–62.

Carandini, M., Heeger, D.J., and Movshon, J.A. (1997). Linearity and normalization in simple cells of the macaque primary visual cortex. J. Neurosci. *17*, 8621–8644.

Carandini, M., Heeger, D.J., and Senn, W. (2002). A synaptic explanation of suppression in visual cortex. J. Neurosci. *22*, 10053–10065.

Chapman, B., Zahs, K.R., and Stryker, M.P. (1991). Relation of cortical cell orientation selectivity to alignment of receptive fields of the geniculocortical afferents that arborize within a single orientation column in ferret visual cortex. J. Neurosci. *11*, 1347–1358.

Choi, V., and Priebe, N.J. (2020). Interocular velocity cues elicit vergence eye movements in mice. J. Neurophysiology *124*, 623–633.

Cohen-Kashi Malina, K., Mohar, B., Rappaport, A.N., and Lampl, I. (2016). Local and thalamic origins of correlated ongoing and sensory-evoked cortical activities. Nat. Commun. *7*, 12740.

Cossell, L., Iacaruso, M.F., Muir, D.R., Houlton, R., Sader, E.N., Ko, H., Hofer, S.B., and Mrsic-Flogel, T.D. (2015). Functional organization of excitatory synaptic strength in primary visual cortex. Nature *518*, 399–403.

DeAngelis, G.C., Robson, J.G., Ohzawa, I., and Freeman, R.D. (1992). Organization of suppression in receptive fields of neurons in cat visual cortex. J. Neurophysiol. *68*, 144–163.

Ferster, D., Chung, S., and Wheat, H. (1996). Orientation selectivity of thalamic input to simple cells of cat visual cortex. Nature *380*, 249–252.

Freeman, T.C., Durand, S., Kiper, D.C., and Carandini, M. (2002). Suppression without inhibition in visual cortex. Neuron *35*, 759–771.

Gilbert, C.D., and Wiesel, T.N. (1990). The influence of contextual stimuli on the orientation selectivity of cells in primary visual cortex of the cat. Vision Res. *30*, 1689–1701.

Goldey, G.J., Roumis, D.K., Glickfeld, L.L., Kerlin, A.M., Reid, R.C., Bonin, V., Schafer, D.P., and Andermann, M.L. (2014). Removable cranial windows for long-term imaging in awake mice. Nat. Protocols *9*, 2515–2538.

Grubb, M.S., and Thompson, I.D. (2003). Quantitative characterization of visual response properties in the mouse dorsal lateral geniculate nucleus. J. Neurophysiol. *90*, 3594–3607.

Gu, Y., and Cang, J. (2016). Binocular matching of thalamocortical and intracortical circuits in the mouse visual cortex. eLife *5*, 1–14.

Guan, S.C., Zhang, S.-H., Zhang, Y.C., Tang, S.M., and Yu, C. (2020). Plaid Detectors in Macaque V1 Revealed by Two-Photon Calcium Imaging. Curr. Biol. *30*, 934–940.e3.

Heeger, D.J. (1992). Normalization of cell responses in cat striate cortex. Vis. Neurosci. *9*, 181–197.

Hofer, S.B., Ko, H., Pichler, B., Vogelstein, J., Ros, H., Zeng, H., Lein, E., Lesica, N.A., and Mrsic-Flogel, T.D. (2011). Differential connectivity and response dynamics of excitatory and inhibitory neurons in visual cortex. Nat. Neurosci. *14*, 1045–1052.

Hubel, D.H., and Wiesel, T.N. (1962). Receptive fields, binocular interaction and functional architecture in the cat's visual cortex. J. Physiol. *160*, 106–154.

Ji, X.Y., Zingg, B., Mesik, L., Xiao, Z., Zhang, L.I., and Tao, H.W. (2016). Thalamocortical Innervation Pattern in Mouse Auditory and Visual Cortex: Laminar and Cell-Type Specificity. Cereb. Cortex *26*, 2612–2625.

Jia, H., Rochefort, N.L., Chen, X., and Konnerth, A. (2010). Dendritic organization of sensory input to cortical neurons in vivo. Nature *464*, 1307–1312.

Jin, J., Wang, Y., Swadlow, H.A., and Alonso, J.M. (2011). Population receptive fields of ON and OFF thalamic inputs to an orientation column in visual cortex. Nat. Neurosci. *14*, 232–238.

Juavinett, A.L., and Callaway, E.M. (2015). Pattern and Component Motion Responses in Mouse Visual Cortical Areas. Curr. Biol. *25*, 1759–1764.

Kerlin, A.M., Andermann, M.L., Berezovskii, V.K., and Reid, R.C. (2010). Broadly tuned response properties of diverse inhibitory neuron subtypes in mouse visual cortex. Neuron *67*, 858–871.

King, J.L., Lowe, M.P., Stover, K.R., Wong, A.A., and Crowder, N.A. (2016). Adaptive processes in Thalamus and cortex revealed by silencing of primary visual cortex during contrast adaptation. Curr. Biol. *26*, 1295–1300.

Koelling, M., Shapley, R., and Shelley, M. (2008). Retinal and cortical nonlinearities combine to produce masking in V1 responses to plaids. J. Comput. Neurosci. *25*, 390–400.

Kondo, S., and Ohki, K. (2016). Laminar differences in the orientation selectivity of geniculate afferents in mouse primary visual cortex. Nat. Neurosci. *19*, 316–319.

Li, Y.-T., Ibrahim, L.A., Liu, B.-H., Zhang, L.I., and Tao, H.W. (2013). Linear transformation of thalamocortical input by intracortical excitation. Nat. Neurosci. *16*, 1324–1330.

Li, B., Thompson, J.K., Duong, T., Peterson, M.R., and Freeman, R.D. (2006). Origins of cross-orientation suppression in the visual cortex. J. Neurophysiol. *96*, 1755–1764.

Lien, A.D., and Scanziani, M. (2013). Tuned thalamic excitation is amplified by visual cortical circuits. Nat. Neurosci. *16*, 1315–1323.

Liu, B.H., Li, P., Li, Y.T., Sun, Y.J., Yanagawa, Y., Obata, K., Zhang, L.I., and Tao, H.W. (2009). Visual receptive field structure of cortical inhibitory neurons revealed by two-photon imaging guided recording. J. Neurosci. *29*, 10520–10532.

Liu, B.H., Li, P., Sun, Y.J., Li, Y.T., Zhang, L.I., Tao, H.W., and Ya-Tang, L. (2010). Intervening inhibition underlies simple-cell receptive field structure in visual cortex. Nat. Neurosci. *13*, 89–96.

Ma, W.P., Liu, B.H., Li, Y.T., Huang, Z.J., Zhang, L.I., and Tao, H.W. (2010). Visual representations by cortical somatostatin inhibitory neurons–selective but with weak and delayed responses. J. Neurosci. *30*, 14371–14379.

Madisen, L., Zwingman, T.A., Sunkin, S.M., Oh, S.W., Zariwala, H.A., Gu, H., Ng, L.L., Palmiter, R.D., Hawrylycz, M.J., Jones, A.R., et al. (2010). A robust and high-throughput Cre reporting and characterization system for the whole mouse brain. Nat. Neurosci. *13*, 133–140.

Marr, D. (1982). Vision: A Computational Investigation into the Human Representation and Processing of Visual Information (W.H. Freeman and Co.).

Marr, D., and Poggio, T. (1976). From Understanding Computation to Understanding Neural Circuitry. Technical Report (Massachusetts Institute of Technology).

Morrone, M.C., Burr, D.C., and Maffei, L. (1982). Functional implications of cross-orientation inhibition of cortical visual cells. I. Neurophysiological evidence. Proc. R. Soc. Lond. B Biol. Sci. *216*, 335–354.

Morrone, M.C., Burr, D.C., and Speed, H.D. (1987). Cross-orientation inhibition in cat is GABA mediated. Exp. Brain Res. *67*, 635–644.

Muir, D.R., Roth, M.M., Helmchen, F., and Kampa, B.M. (2015). Model-based analysis of pattern motion processing in mouse primary visual cortex. Front. Neural Circuits *9*, 38.

Muir, D.R., Molina-Luna, P., Roth, M.M., Helmchen, F., and Kampa, B.M. (2017). Specific excitatory connectivity for feature integration in mouse primary visual cortex. PLoS Comput. Biol. *13*, e1005888.

Nelson, J.I., and Frost, B.J. (1978). Orientation-selective inhibition from beyond the classic visual receptive field. Brain Res. *139*, 359–365.

Niell, C.M., and Stryker, M.P. (2008). Highly selective receptive fields in mouse visual cortex. J. Neurosci. *28*, 7520–7536.

Ozeki, H., Finn, I.M., Schaffer, E.S., Miller, K.D., and Ferster, D. (2009). Inhibitory stabilization of the cortical network underlies visual surround suppression. Neuron *62*, 578–592.

Palagina, G., Meyer, J.F., and Smirnakis, S.M. (2017). Complex Visual Motion Representation in Mouse Area V1. J. Neurosci. *37*, 164–183.

Park, H.N., Qazi, Y., Tan, C., Jabbar, S.B., Cao, Y., Schmid, G., and Pardue, M.T. (2012). Assessment of axial length measurements in mouse eyes. Optometry and Vision Science *89*, 296.

Pattadkal, J.J., Mato, G., van Vreeswijk, C., Priebe, N.J., and Hansel, D. (2018). Emergent Orientation Selectivity from Random Networks in Mouse Visual Cortex. Cell Rep. *24*, 2042–2050.e6.

Pelli, D.G. (1997). The VideoToolbox software for visual psychophysics: Transforming numbers into movies. Spatial Vision *10*, 437–442.

Piscopo, D.M., El-Danaf, R.N., Huberman, A.D., and Niell, C.M. (2013). Diverse visual features encoded in mouse lateral geniculate nucleus. J. Neurosci. *33*, 4642–4656.

Priebe, N.J., and Ferster, D. (2006). Mechanisms underlying cross-orientation suppression in cat visual cortex. Nat. Neurosci. *9*, 552–561.

Priebe, N.J., and Ferster, D. (2012). Mechanisms of neuronal computation in mammalian visual cortex. Neuron *75*, 194–208.

Priebe, N.J., Mechler, F., Carandini, M., and Ferster, D. (2004). The contribution of spike threshold to the dichotomy of cortical simple and complex cells. Nat. Neurosci. *7*, 1113–1122.

Reid, R.C., and Alonso, J.M. (1995). Specificity of monosynaptic connections from thalamus to visual cortex. Nature *378*, 281–284.

Reig, R., Gallego, R., Nowak, L.G., and Sanchez-Vives, M.V. (2006). Impact of cortical network activity on short-term synaptic depression. Cereb. Cortex *16*, 688–695.

Reinhold, K., Lien, A.D., and Scanziani, M. (2015). Distinct recurrent versus afferent dynamics in cortical visual processing. Nat. Neurosci. *18*, 1789–1797.

Ringach, D.L. (2019). The geometry of masking in neural populations. Nat. Commun. *10*, 4879.

Ringach, D.L., Shapley, R.M., and Hawken, M.J. (2002). Orientation selectivity in macaque V1: diversity and laminar dependence. J. Neurosci. *22*, 5639–5651.

Rubin, D.B., Van Hooser, S.D., and Miller, K.D. (2015). The stabilized supralinear network: a unifying circuit motif underlying multi-input integration in sensory cortex. Neuron *85*, 402–417.

Runyan, C.A., Schummers, J., Van Wart, A., Kuhlman, S.J., Wilson, N.R., Huang, Z.J., and Sur, M. (2010). Response features of parvalbumin-expressing interneurons suggest precise roles for subtypes of inhibition in visual cortex. Neuron *67*, 847–857.

Runyan, C.A., and Sur, M. (2013). Response selectivity is correlated to dendritic structure in parvalbumin-expressing inhibitory neurons in visual cortex. J. Neurosci. *33*, 11724–11733.

Sanchez-Vives, M.V., Nowak, L.G., and McCormick, D.A. (2000). Membrane mechanisms underlying contrast adaptation in cat area 17 in vivo. J. Neurosci. *20*, 4267–4285.

Scholl, B., Tan, A.Y., Corey, J., and Priebe, N.J. (2013). Emergence of orientation selectivity in the Mammalian visual pathway. J. Neurosci. *33*, 10616–10624.

Scholl, B., Pattadkal, J.J., Dilly, G.A., Priebe, N.J., and Zemelman, B.V. (2015). Local Integration Accounts for Weak Selectivity of Mouse Neocortical Parvalbumin Interneurons. Neuron *87*, 424–436.

Sengpiel, F., Baddeley, R.J., Freeman, T.C., Harrad, R., and Blakemore, C. (1998). Different mechanisms underlie three inhibitory phenomena in cat area 17. Vision Res. *38*, 2067–2080.

Sohya, K., Kameyama, K., Yanagawa, Y., Obata, K., and Tsumoto, T. (2007). GABAergic neurons are less selective to stimulus orientation than excitatory neurons in layer II/III of visual cortex, as revealed by in vivo functional Ca2+ imaging in transgenic mice. J. Neurosci. *27*, 2145–2149.

Sokal, R.R., and Rohlf, F.J. (1995). Biometry. The Principles and Practice of Statistics in Biological (New York: Research WH Freeman and Company).

Suresh, V., Çiftçioğlu, U.M., Wang, X., Lala, B.M., Ding, K.R., Smith, W.A., Sommer, F.T., and Hirsch, J.A. (2016). Synaptic Contributions to Receptive Field Structure and Response Properties in the Rodent Lateral Geniculate Nucleus of the Thalamus. J. Neurosci. *36*, 10949–10963.

Tan, A.Y., Brown, B.D., Scholl, B., Mohanty, D., and Priebe, N.J. (2011). Orientation selectivity of synaptic input to neurons in mouse and cat primary visual cortex. J. Neurosci. *31*, 12339–12350.

Tan, A.Y., Chen, Y., Scholl, B., Seidemann, E., and Priebe, N.J. (2014). Sensory stimulation shifts visual cortex from synchronous to asynchronous states. Nature *509*, 226–229.

Tring, E., and Ringach, D.L. (2018). On the subspace invariance of population responses. *arXiv*, arXiv:1811.03251.

Wilson, N.R., Runyan, C.A., Wang, F.L., and Sur, M. (2012). Division and subtraction by distinct cortical inhibitory networks in vivo. Nature *488*, 343–348.

Zhao, X., Chen, H., Liu, X., and Cang, J. (2013). Orientation-selective responses in the mouse lateral geniculate nucleus. J. Neurosci. *33*, 12751–12763.

STAR★METHODS

KEY RESOURCES TABLE

REAGENT or RESOURCE	SOURCE	IDENTIFIER
Bacterial and virus strains		
AAV1.Syn.Flex.GCaAMP6s.WPRE.SV40	UPenn	CS1242
Experimental models: Organisms/strains		
Mouse: C57BL/6J	Jackson Labs	000664
Mouse: Cre dependent ChR2-EYFP	Jackson Labs	024109
Mouse: PV-Cre knockin	Scholl et al., 2015	N/A
Mouse: Ai162 transgenic GCaMP6s	Jackson Labs	031562
Mouse: Slc17a7-IRES2-Cre-D	Jackson Labs	005628
Mouse: Pvalb-IRES-Cre	Jackson Labs	017320
Deposited data		
Electrophysiology and imaging data	This paper	https://doi.org/10.6084/m9.figshare.c.5677225.v1
Software and algorithms		
MATLAB	Mathworks	https://www.mathworks.com/products/matlab.html
Labview	National Instruments	https://www.ni.com/en-us/shop/labview.html
Scanbox	Neurolabware	https://scanbox.org/tag/neurolabware/
MWorks	MWorks	https://mworks.github.io/
Custom MATLAB scripts	This paper	https://doi.org/10.6084/m9.figshare.c.5677225.v1

RESOURCE AVAILABILITY

Lead contact

Further information and requests for resources and reagents should be directed to Lindsey Glickfeld (glickfeld@neuro.duke.edu).

Materials availability

No new reagents were generated as a result of this study.

Data and code availability

- All electrophyisology and imaging data included in the manuscript figures are available on Figshare. A link is provided in the key resources table.
- All original code needed to generate the manuscript figures (including the model) is available on Figshare. A link is provided in the key resources table.
- Any additional information required to reanalyze the data reported in this paper is available from the lead contact upon request.

EXPERIMENTAL MODEL AND SUBJECT DETAILS

Animals

Electrophysiology

Experiments were conducted using adult C57/BL6J (Jackson Labs #000664) mice of both sexes (n = 20). For inactivation experiments, parvalbumin (PV)-Cre knockin mice (Scholl et al., 2015) were crossed to a Cre dependent channelrhodopsin-2 (ChR2)-EYFP strain (Jackson Labs #024109, Madisen et al., 2010, n = 13). These progenies selectively express ChR2 in PV+ interneurons. Mice were P35 and older to avoid the visual critical period. All animal procedures were approved by the University of Texas at Austin Institutional Animal Care and Use Committee.

Imaging

Experiments were conducted using 18 mice of both sexes older than P60. C57/BL6J was the primary background with up to 50% CBA/CaJ (Jackson Labs #000654). GCaMP6 was expressed either transgenically (Ai162 [tm162.1(tetO-GCaMP6s,CAG-tTA2)Hze; Jackson Labs #031562] crossed to Slc17a7-IRES2-Cre-D [tm1.1(Cre)Hze; Jackson Labs #023527], n = 10) or virally

(Emx1-IRES-Cre [tm1(cre)Krj, Jackson Labs # 005628], n = 3; Pvalb-IRES-Cre [tm1(cre)Arbr, Jackson Labs #017320], n = 5). All animal procedures were approved by Duke University Institutional Animal Care and Use Committee.

METHOD DETAILS

Electrophysiology

Surgery

Procedures for mouse electrophysiology recordings are based on those previously described (Scholl et al., 2013). Mice were anesthetized with 1,000 mg/kg urethane and 10 mg/kg chlorprothixene via intraperitoneal injection. A further intraperitoneal injection of 20 mg/kg dexamethasone was administered to prevent brain edema. During the course of the experiment, body temperature was monitored and maintained at 37°C. A tracheotomy was performed and the head was placed in a mouse adaptor (Stoelting). A small craniotomy (~2-3 mm^2) and durotomy were performed over the appropriate area of the sensory cortex. V1 was located by multiunit extracellular recordings with tungsten electrodes (1MΩ, Micro Probes). Mouse eyes were kept moist with a thin layer of silicone oil. The cortical surface was kept moist with saline or 4% agarose in normal saline.

Whole cell recordings

We performed in-vivo whole cell recordings using the blind patch method. A silver-silver chloride wire was inserted into muscle near the base of the skull and used as a reference electrode. Pipettes (5-10 MΩ) were pulled from 1.2 mm outer diameter, 0.7 mm inner diameter KG-33 borosilicate glass capillaries (King Precision Glass) on a P-2000 micropipette puller (Sutter Instruments). Pipettes were filled with (in mM) 135 K-gluconate, 4 NaCl, 0.5 EGTA, 2 MgATP, 10 phosphocreatine disodium, and 10 HEPES, pH adjusted to 7.3 with KOH(Sigma-Aldrich). Neurons were recorded 150-500 μm below the cortical surface. Recordings were performed with a MultiClamp 700B patch clamp amplifier (Molecular Devices). Current flow out of the amplifier into the patch pipette was considered positive.

Extracellular recording

For extracellular recordings, electrodes (1-2MΩ, Micro Probes) were lowered into the LGN (2.5 mm posterior of bregma and 2 mm lateral of midline) with a motorized drive (MP-285, Sutter Instrument). The LGN was located at a depth between 2.2-2.8 mm (Grubb and Thompson, 2003). Action potentials were identified and isolated using a dual window discriminator (Bak Electronics, DDIS-1) and the timing of each spike and the raw extracellular trace were recorded for later analysis.

Cortical Inactivation

Records for inactivation experiments were restricted to layer 4, defined as 350-500 μm below the surface. A 470-nm fiber-coupled LED light was used to activate ChR2 in PV+ neurons. The light covered the entire craniotomy and the light intensity was between 1 and 1.3 mW. The light was turned on 250 ms before the onset of visual stimulation.

Imaging

Surgery

Animals were implanted with a titanium headpost and 5 mm cranial window as previously described (Goldey et al., 2014). Briefly, dexamethasone (3.2 mg/kg, s.c.) and Meloxicam (2.5 mg/kg, s.c.) were administered at least 2 h before surgery. Animals were anesthetized with ketamine (200 mg/kg, i.p.), xylazine (30 mg/kg, i.p.) and isoflurane (1.2%–2% in 100% O2). Using aseptic technique, a headpost was secured using cyanoacrylate glue and C&B Metabond (Parkell), and a 5 mm craniotomy was made over the left hemisphere (center: 2.8 mm lateral, 0.5 mm anterior to lambda) allowing implantation of a glass window (an 8-mm coverslip bonded to two 5-mm coverslips (Warner no. 1) with refractive index-matched adhesive (Norland no. 71)) using Metabond.

The mice were allowed to recover for one week before habituation to head restraint. Habituation to head restraint increased in duration from 15 min to > 2 h over 1-2 weeks. During habituation and imaging, mice were head restrained while allowed to freely run on a circular disc (InnoWheel, VWR).

Mapping

Retinotopic maps were generated from GCaMP fluorescence or intrinsic autofluorescence. For intrinsic autofluorescence, the brain was illuminated with blue light (473 nm LED (Thorlabs) or a white light source (EXFO) with a 462 ± 15 nm band pass filter (Edmund Optics)), and emitted light was measured through a green and red filter (500 nm longpass). For GCaMP imaging, the same excitation light was used, but emitted light was measured through a 520 ± 18 nm band pass filter. For all conditions, images were collected using a CCD camera (Rolera EMC-2, Qimaging) at 2 Hz through a 5x air immersion objective (0.14 numerical aperture (NA), Mitutoyo), using Micromanager acquisition software (NIH). Images were analyzed in ImageJ (NIH) to measure changes in fluorescence (dF/F; with F being the average of all frames) to identify V1 and the HVAs, so as to target viral injections and/or imaging sessions to a monocular region of V1.

Viral injection

We targeted V1 in EMX1::Cre and PV::Cre mice for viral expression of GCaMP6s. Dexamethasone (3.2 mg/kg, s.c.) was administered at least 2 h before surgery and animals were anesthetized with isoflurane (1.2%–2% in 100% O2). The coverslip was sterilized with 70% ethanol and the cranial window removed. A glass micropipette was filled with virus (AAV1.Syn.Flex.GCaMP6s.WPRE.SV40; titer: 1-3e13 GC/ml; UPenn CS1242), mounted on a Hamilton syringe, and lowered into the brain. 100 nL of virus was injected at 250 and 500 μm below the pia (30 nL/min); the pipette was left in the brain for an additional 10 minutes to allow the virus to infuse

into the tissue. Following injection, a new coverslip was sealed in place. Imaging experiments were conducted at least one week following injection to allow for sufficient expression.

Two-photon imaging

Calcium imaging data was collected using a microscope controlled by Scanbox software (Neurolabware). Excitation light (920 nm) from a Mai Tai eHP DeepSee laser (Newport) was directed into a modulator (Conoptics) and raster scanned onto the brain with a resonant galvanometer (8 kHz, Cambridge Technology) through a 16X (0.8 NA, Nikon) water-immersion lens. Average power at the surface of the brain was 30-50 mW. Frames were collected either at 15 Hz (FOV of 680x605 μm) or at 30 Hz (415x735 μm). Emitted photons were directed through a green filter (510 ± 42 nm band filter; Semrock) onto GaAsP photomultipliers (H10770B-40, Hamamatsu). Images of excitatory cells were captured 193.7 ± 31.3 μm (range: 150-250 μm) below the pia, while inhibitory cells were imaged at 183.3 ± 12.4 μm (range: 150-225 μm).

Eye tracking

Pupil position was monitored via scattered infrared light from two-photon imaging. Light was collected using a GENIE Nano CMOS camera (Teledyne Dalsa) using a long-pass filter (695 nm) at the imaging frame rate.

Stimulus Presentation

Electrophysiology

All stimuli were generated via the Psychophysics Toolbox (Brainard, 1997; Pelli, 1997) for MATLAB (Mathworks) on a Macintosh (Apple) computer. Stimuli were presented on a calibrated CRT monitor (Sony FDM-520) placed 25 cm in front of the animals' eyes with a refresh rate of 100 Hz and a spatial resolution of 1,204 X 768 pixels. The mean luminance of the monitor was 40 cd/m^2. Drifting gratings (at the preferred spatial frequency, temporal frequency of 2 Hz) were presented for a period of 4 s. Grating size was tailored for each neuron to only engage the center receptive field. Each stimulus was followed by a 1 s blank period. Test and mask gratings were presented at all combinations of four contrasts: 0%, 16%, 32% and 48%. For the phase shift experiments, the spatial phase of the test stimulus was fixed at 0° while the mask initial spatial phase was set to one of four phases: 0°, 90°, 180°, 270°. In a subset of neurons (n = 3) 8 spatial phases 45° apart were presented. For a subset of LGN recordings a higher mask spatial frequency was used (10 Hz).

Imaging

Visual stimuli were presented on a 144-Hz (Asus) LCD monitor for imaging experiments. The monitor was calibrated with an i1 Display Pro (X-rite) for mean luminance at 50 cd/m^2 and positioned 21 cm from the eye. All stimulus presentations used MWorks (https://mworks.github.io/) and custom software in MATLAB (MathWorks). All visual stimulus conditions within each experiment were randomly interleaved.

Visual stimuli were sinusoidal drifting gratings, 30 deg in diameter with a gabor mask, placed in the monocular visual field. Five different visual stimulus protocols were used for the imaging experiments. A) ''All directions plus mask'': Drifting gratings moving in 16 directions with and without an orthogonal mask (starting phase of 0° or 90°) at 50% contrast. Stimuli were presented for 1 s, with a 3 s mean luminance inter-trial interval (ITI), at a spatial frequency (SF) of 0.05 cycles/degree and a temporal frequency (TF) of 2 Hz. Data from 7 mice were collected from these experiments and are presented in Figure 1. B) ''Two directions plus mask at 4 phases'': Drifting gratings moving rightward or upward each at three contrasts (0, 32 and 48%). The upward drifting grating was presented at 4 phases (0, 90, 180, or 270°). Stimuli were presented for 4 s, with a 4 s ITI, at a SF of 0.05 cycles/degree and a TF of 1 Hz. Data from 8 mice were collected from these experiments and are presented in Figure 6, 7 and 8. C) ''Two directions plus mask at 8 phases'': Drifting gratings moving rightward at 0 and either 32% or 48% contrast and upward at 0 and 48% contrast. The upward drifting grating was presented at 8 phases 45° apart. Stimulus duration, SF and TF were the same as in protocol B. These experiments were followed by a separate run in which we presented drifting gratings moving in 16 directions at matched SF and TF and 100% contrast. Data from 7 mice were collected from these experiments and are presented in Figures 6, 7, and 8. D) ''Stimulus adaptation'': Drifting gratings moving rightward or upward at each of five contrasts (0 6.25, 12.5, 25, 50%), either with or without adaptation. Adaptation was performed in blocks of 60 trials; adaptation blocks were preceded by a 2 min presentation of a 50% contrast, rightward drifting grating, followed by a 5 s top-up before each trial. The timing of the control block was the same, but the screen was at mean luminance. Test stimuli were presented for 1 s, at a SF of 0.1 cycles/degree and a TF of 2 Hz. Data from 7 mice were collected from these experiments and are presented in Figure 2. E) ''Two directions plus mask at 4 phases and 2 TF'': Drifting gratings moving rightward or upward each at two contrasts (0 and 48%). The upward drifting grating was presented at 4 phases (0, 90, 180, or 270°) and 2 TFs (1 and 5 Hz), while the rightward drifting grating was always at 1 Hz. Stimuli were presented for 4 s, with a 4 s ITI, at a SF of 0.05 cycles/degree. Data from 2 mice were collected from these experiments and are presented in Figure S5.

Feedforward Model

The model was adapted from a previous study (see details: Priebe and Ferster, 2006). Thalamic neurons were modeled as a single ON subregion for simplicity. To mimic the lower firing rates observed in mice, the firing rates were set to 7.3-11.3 Hz with a background firing rate of 0-2 Hz. The receptive fields of 8 thalamic relay cells were aligned along the preferred orientation of the neuron. To adjust the orientation selectivity of the model, the space between the receptive fields was systematically reduced (max = pi/4; min = 0). To simulate populations of model neurons, neurons were randomly assigned a value in this range. To mimic experimental conditions, the values of the test and mask phase were randomly assigned a value between 1° and 360°.

To generate random model neurons, 8 afferent receptive fields were each assigned a random vertical and horizontal position within a 25 × 25 degree square from a flat distribution. The preferred orientation was then found by running model simulation in increments of 22.5 degrees. All analyses are performed at the preferred test and orthogonal mask stimulus condition.

QUANTIFICATION AND STATISTICAL ANALYSIS

Electrophysiology

Records were analyzed by using a 5-ms median filter to remove action potentials to isolate the membrane potential and spiking responses. Membrane potential and spiking responses were cycle averaged after removing the first cycle. We used the Fourier transform to calculate the mean and modulation amplitude for membrane potential and spiking responses.

To predict spike rates from membrane potential records, data were fit with the following equation:

$$R(V_m) = k[V_m - V_{rest}]$$

where R is spike rate, V_m is membrane potential, V_{rest} is baseline membrane potential and + indicates rectification.

Imaging

Two-photon analysis

All two-photon imaging data was analyzed using custom code written in MATLAB (Mathworks). Image stacks from each imaging session were registered for x-y motion to the same stable reference image selected out of several 500-frame-average images, using Fourier domain subpixel 2D rigid body registration.

Cell bodies were manually segmented from the average change in fluorescence (dF/F) during stimulus presentation (where F is the average of 1 s preceding the stimulus) for each unique stimulus condition as well as the maximum projection across all stimulus conditions. Fluorescence time courses were generated by averaging all pixels in a cell mask. Neuropil signals were removed by first selecting a shell around each neuron (excluding neighboring neurons), estimating the neuropil scaling factor (by maximizing the skew of the resulting subtraction), and removing this component from each cell's time course. Visually evoked responses were measured as the average dF/F during the stimulus presentation window, excluding the five frames immediately following stimulus onset to account for visual conduction delays. Cells were categorized as visually responsive if they had statistically significant responses to at least one stimulus condition compared to a similar baseline window, as measured with a one-sided t test with the significance threshold Bonferroni corrected for the number of stimulus conditions. The preferred direction was determined by averaging across stimuli of the same direction and identifying the stimulus condition that drove the strongest response.

Masking index (MI) and selectivity index (SI) were only measured for conditions where the neuron responded significantly to either the test or the mask alone. For calculating MI, SI, and orientation selectivity index (OSI) responses below zero were set to zero, such that all values are constrained to be between 0 and 1. Cells with significant MI in the control condition (Figure 2) were determined with a two-way Student's t test comparing the distribution of plaid responses across trials to the sum of the average test and mask response.

Locomotion and eye tracking analysis

Locomotion was monitored with a digital encoder (US Digital) attached to a circular running wheel. In general, the mice were stationary and only ran (average speed greater than 2 cm/s) on a minority of trials (average: 3.6%, median: 0.8%; range 0%–45%, 24 sessions). Thus, we combined all trials regardless of locomotion state.

We used pupil diameter as an alternative measure of arousal. Pupil size and position were extracted from each frame using the native MATLAB function imfindcircles and quantified for each trial by averaging all frames during each stimulus presentation. To determine if there is a relationship between arousal and MI, we identified the trials from experiments from stimulus set C (since this had the smallest number of stimulus conditions) within the bottom (0.17 ± 0.01 mm, n = 7 mice) and top (0.27 ± 0.02 mm) quartile of pupil size. This increase in pupil diameter resulted in a significant increase in response to the gratings (bottom- 0.19 ± 0.01; top- 0.34 ± 0.02; n = 272 cells; paired t test: p = 9.9e-15), but no significant change in MI (bottom- 0.03 ± 0.03; top- −0.01 ± 0.03; p = 0.21).

To ensure that variable pupil position did not obscure the phase sensitivity of visual responses, average pupil position was quantified for these experiments (Figures 6, 7, and 8). The average pupil position during each stimulus presentation was converted to degrees of visual angle with a 1:25 degrees to micrometer scale (Park et al., 2012). Only trials in which the pupil was within 2 deg of the median position were considered for analysis.

Phase sensitivity analysis.

To measure the phase dependence, the masking index data were fit with a sinusoid:

$$R = b + A * \frac{\sin(2 * \pi * \Phi)}{Per * 2 * \pi * Pha}$$

where b is the baseline offset, A is the amplitude, Per is the period, and Pha is the preferred phase. Shuffled fits were performed on data in which the phase-identity of trials was randomized. For electrophysiology data this was done on a cycle as opposed to a trial basis, and standard error for MI (Figure 6) were computed using the bootstrap technique (Sokal and Rohlf, 1995).